Ref. 3, p. 325.

[15]P. J. Lin and D. L. Mitchell (private communication). This dispersion relation has also been used by G. A. Antcliffe.

[16]J. O. Dimmock has pointed out that there are less restrictive approximations than we have made to Eqs. (15) or (16) which also yield an ellipsoidal model with $K=(P_\perp/P_\parallel)^2$. The most general of these is obtained by setting $P_\perp^2/P_\parallel^2=m_\parallel^v/m_\perp^v=m_\parallel^c/m_\perp^c$.

[17]B. Lax, J. G. Mavroides, H. J. Zeiger, and R. J. Keyes, Phys. Rev. 122, 31 (1961).

[18]L. M. Roth, Phys. Rev. 145, 434 (1966).

[19]J. F. Butler and A. R. Calawa, in *Physics of Quantum Electronics*, edited by P. L. Kelley, B. Lax, and P. E. Tannenwald (McGraw-Hill, New York, 1966), pp. 458-466.

[20]C. K. N. Patel and R. E. Slusher, Phys. Rev. 177, 1200 (1969).

[21]L. M. Roth, Phys. Rev. 118, 1534 (1960).

PHYSICAL REVIEW B VOLUME 2, NUMBER 6 15 SEPTEMBER 1970

Luminescence and Minority Carrier Recombination in p-Type GaP(Zn,O)

J. M. Dishman, M. DiDomenico, Jr., and R. Caruso

Bell Telephone Laboratories, Murray Hill, New Jersey 07974

(Received 16 April 1970)

A detailed study of luminescence and minority carrier recombination in Zn- and O-doped p-GaP is presented. To interpret the results of photoluminescence measurements, a three-path model for minority carrier recombination is developed. This model includes recombination through nearest-neighbor Zn-O complexes, isolated O donors, and an unspecified shunt path. Included in the model are the effects of thermalization of electrons trapped on Zn-O centers and the effects of plasma screening by free holes on excitons bound to these centers. These processes together with nonradiative Auger recombination of excitons and trapped electrons at Zn-O complexes provide the major limitation of the red quantum efficiency in GaP-(Zn, O). Using an iterative self-consistent fit to the available temperature and Zn-doping dependence of the red luminescence efficiency and time decay, values are obtained for all of the important capture cross sections, time decay parameters, and Auger recombination coefficients, as well as the minority carrier lifetime. In addition, the concentrations of the deep Zn-O and O centers are measured optically. It is concluded that the bulk quantum efficiency of GaP(Zn,O) can be improved by simultaneously increasing the minority carrier lifetime and decreasing the free-hole concentration (and consequent Auger processes) by compensation.

I. INTRODUCTION

Two deep radiative recombination centers are introduced into GaP by the simultaneous presence of zinc and oxygen impurities. Isolated oxygen is a deep donor approximately 0.9 eV below the conduction band.[1] Infrared radiative recombination at oxygen ($h\nu \approx 1.35$ eV) occurs when trapped electrons recombine either with holes trapped on isolated zinc acceptors[1] or with free holes.[2] The isoelectronic center formed by a zinc acceptor and an oxygen donor on nearest-neighbor sites (Zn-O complex) also acts as a deep electron trap approximately 0.2–0.3 eV below the conduction band.[3,4] Red luminescence ($h\nu \approx 1.77$ eV) originates from Zn-O centers in two ways: (i) by pair recombination of trapped electrons with holes on distant Zn acceptors and (ii) by recombination of bound excitons. At room temperature, the red luminescence is essentially excitonic,[4] whereas the infrared luminescence is essentially free to bound.[2]

In a previous paper[5] (hereafter referred to as I), a general model for the recombination kinetics of electrons and holes at isoelectronic centers was developed. This model considered in detail the three occupation states of the isoelectronic center, i.e., empty, electron (hole) occupied, and exciton occupied. It therefore generalized the conventional two-state Shockley-Read-Hall[6] (SRH) recombination model applicable to nonisoelectronic centers. In the present paper we study minority carrier recombination in p-type Zn- and O-doped GaP by photoluminescence techniques. A three-path model for the minority carrier recombination in presented.[7] This model includes recombination through the isoelectronic Zn-O complex, the deep O donor, and an unspecified "shunt path" which accounts for all other nonradiative centers. The results derived in I are applied in describing recombination through the Zn-O luminescent center. In this treatment we also consider explicitly how the recombination mechanisms associated with the Zn-O center are modified

by plasma screening of the valence-band holes. The influence of screening in GaP(Zn, O) has been discussed elsewhere.[8] In this paper it is shown by comparison with experimental data that plasma screening markedly affects the recombination processes through the Zn-O complex.

We have previously shown[5] that thermalization of bare electrons trapped on Zn-O complexes has an important influence on the time decay of the red luminescence at room temperature and above. Other treatments[7] of the steady-state kinetics in GaP(Zn,O) have neglected this effect. Based on an iterative self-consistent analysis of the temperature and doping dependences of the quantum efficiency and decay time of the red luminescence from GaP(Zn, O), we find that the best value for the room-temperature trap depth of the Zn-O complex is $E_t \approx 0.23$ eV.[9] Spectral results are not in disagreement with this value.[10] In addition we find the room-temperature cross section for capture of electrons onto Zn-O centers is $\sigma_{nt} \approx 2\times10^{-16}$ cm^{-2}.[11] These values make thermalization an important process in limiting the ultimate room-temperature quantum efficiency and time decay in GaP(Zn, O). A second limiting process is nonradiative Auger recombination of bound excitons and trapped electrons. We find that Auger processes typically account for 90% of the recombination at Zn-O complexes.[5,12] On the basis of these results we suggest that the red luminescence efficiency in GaP(Zn, O) can be improved by increasing the Zn-O nearest-neighbor pairing (i.e., through annealing)[13,14] and by compensation to reduce the free-hole concentration and consequent Auger processes. Changes in the room-temperature luminescence decay time and efficiency with annealing are shown to result primarily from changes in Zn-O trap concentration[15] and the minority carrier lifetime.

Using the three-path recombination model, we derive expressions for the low-level quantum efficiencies and high-level saturation values of the red and infrared luminescence in terms of branching ratios, concentrations of impurities, and lifetimes. On the basis of these expressions, we show how the concentrations of the deep centers Zn-O and O can be determined from a series of five optical measurements: (i) impurity absorption below the band gap, (ii) internal photoluminescence quantum efficiency for below-gap excitation, (iii) internal photoluminescence quantum efficiency for above-gap excitation, (iv) photoluminescence saturation, and (v) decay time of luminescence. Measurements (i)–(iii) determine the branching ratios for capture of minority carriers into the Zn-O and O centers. It is shown that the value of incident excitation for which the photoluminescence saturates is simply related to these branching ratios, the concentrations of the centers, and the lifetimes of minority carriers in these centers. We show that these lifetimes can be deduced from the luminescence decay times in a straightforward way. Hence, measurements (iv) and (v) determine the concentrations of the deep centers when combined with the branching ratio information obtained from measurements (i)–(iii). We point out that measurement (i) can provide estimates of deep center concentrations[4] when used in conjunction with Smakula's equation. In essence, our technique avoids the problem of determining the effective-field ratio by using the experimental data obtained in measurements (ii)–(v).

We also show that the internal photoluminescence quantum efficiency can be determined experimentally from a measurement of the surface radiance using a parallel plane sample geometry.[16] Complicating the interpretation of the internal efficiency measurement is the considerable overlap[17] between the red and infrared luminescence bands for temperatures above 200 °K. We show how the two bands can be separated using below-gap excited photoluminescence spectra and time-decay data.[18] Separate spectra for recombination at Zn-O and O impurities at 300 °K are presented.

A detailed analysis of photoluminescence saturation is presented. In particular, the importance of nonlocal effects due to the exponential falloff and Gaussian character of the laser excitation in taken into account. Theoretical saturation curves parametrized in terms of measured branching ratios are generated[19] for use in determining the saturation value of the luminescence excitation.

Several solution-grown[20] samples of GaP(Zn, O) have been studied. Using the five optical measurements outlined above, Zn-O and O concentrations were found to be typically of order 10^{16} and 10^{17} cm^{-3}, respectively, for crystals prepared by adding 0.07 mol% Zn and 0.02 mol% Ga_2O_3 to the melt. A major fraction of the minority carrier recombination in these crystals is found to proceed through an unidentified nonluminescent center. An important observation is that annealing the samples at 400 and 600 °C increases the Zn-O complex concentration (by as much as a factor of 5); however, recombination through the nonradiative center is found to increase by a factor comparable to the increase in Zn-O complex concentration so that the over-all improvement in luminescent efficiency rarely exceeds 20%.

II. STEADY-STATE RECOMBINATION KINETICS

A. Local Solutions

A schematic representation of the three-path model used in analyzing the recombination kinetics in p-type GaP(Zn, O) is shown in Fig. 1. We first

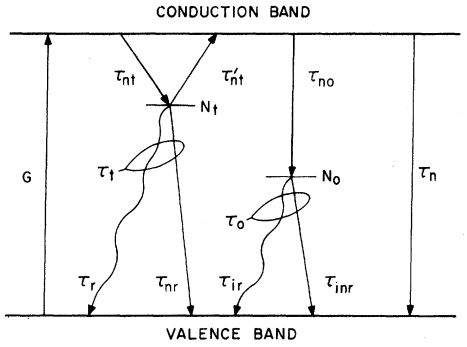

FIG. 1. Schematic representation of the three-path model for recombination of minority carriers in p-type GaP(Zn, O). After generation by the excitation, G minority carriers may be captured by Zn-O centers (τ_{nt}), by oxygen donors (τ_{n0}), or may be shunted to the valence band by unknown residual impurities (τ_n). After capture, electrons at Zn-O sites may be thermalized to the conduction band (τ'_{nt}), or may recombine with holes radiatively (τ_r) or nonradiatively (τ_{nr}). Likewise, electrons trapped at neutral O donors may recombine with holes radiatively (τ_{ir}) or nonradiatively (τ_{inr}). N_t and N_0 are the concentrations of Zn-O and O centers, respectively. The lifetimes τ_t and τ_0 are defined in the text.

consider what happens locally within a small volume of the crystal when electron-hole pairs are generated at a steady-state rate G ($\sec^{-1}\mathrm{cm}^{-3}$) and diffusion of the carriers can be neglected. The generated minority carriers (concentration n) recombine at isoelectronic Zn-O traps (concentration N_t), at oxygen donors (concentration N_0), and through unspecified residual impurities which shunt electrons from conduction band to valence band at a rate n/τ_n. We take the oxygen donor to be a conventional two-state SRH recombination center which captures minority carriers at a rate[21] $(n/\tau_{n0})(1-N_0^0/N_0)$, where N_0^0 is the concentration of neutral oxygen donors and τ_{n0} is the capture lifetime defined by

$$\tau_{n0} \equiv (v\sigma_{n0}N_0)^{-1}. \tag{1}$$

In Eq. (1), v is the thermal velocity of electrons in the conduction band, and σ_{n0} is the electron capture cross section of the ionized oxygen donor. Since oxygen is a deep donor, we neglect thermalization of the captured electrons to the conduction band. Recombination at oxygen centers is then governed by

$$(n/\tau_{n0})(1-N_0^0/N_0) = N_0^0/\tau_0, \tag{2}$$

where τ_0 is the total lifetime of an electron on the neutral donor.

Because the Zn-O isoelectronic centers can exist in three possible states, i.e., empty, electron-occupied, and exciton-occupied, the kinetics of recombination at these centers cannot be treated using the standard two-state SRH model. It was shown previously[5] that the steady-state recombination kinetics for three-state isoelectronic impurities can be treated using a simple modification of the SRH model by defining N_t^e as the concentration of isoelectronic centers occupied by electrons in either single "bare" electron states (concentration N_t^-) or exciton states (concentration N_t^x). The capture rate of minority carriers into the Zn-O traps then becomes $(n/\tau_{nt})(1-N_t^e/N_t)$, with τ_{nt} defined analogously to τ_{n0} [see Eq. (1)]:

$$\tau_{nt} = (v\sigma_{nt}N_t)^{-1}, \tag{3}$$

where σ_{nt} is the cross section for capture of minority carriers by the empty (neutral) state of the complex. The equation describing steady-state recombination at an isoelectronic center differs from the usual SRH expression through a term governing thermalization of trapped electrons. For an isoelectronic center this thermalization rate is (see Appendix A) $(n_t/\tau_{nt})(1-f_0)(N_t^e/N_t)$, where the quantity n_t is defined by

$$n_t \equiv \beta_t N_c e^{-E_t/kT}, \tag{4}$$

and f_0 is the fraction of N_t^e states which are excitonic and is given by[5]

$$f_0 = (1 + p_h/p + N_t\tau_{pt}/p\tau_\alpha)^{-1}. \tag{5}$$

In Eq. (4), N_c is the conduction-band density of states, β_t^{-1} is the degeneracy of the bare-electron state of the complex, E_t is the trap energy measured from the conduction-band edge, and k is the Boltzmann constant. In Eq. (5) (derived previously in Ref. 5), p is the free-hole density and τ_{pt} is the capture lifetime for holes into the negatively charged (bare-electron occupied) complex. This is defined by

$$\tau_{pt} = (v\sigma_{pt}N_t)^{-1}, \tag{6}$$

where σ_{pt} is the screened capture cross section for holes. (Screening of σ_{pt} is discussed in Ref. 8 and in Sec. V of the present paper.) The lifetime τ_α is defined by

$$1/\tau_\alpha = 1/\tau_{xr} + 1/\tau_{xn}, \tag{7}$$

where τ_{xr} is the intrinsic radiative lifetime of excitons bound to the Zn-O complex, and τ_{xn} is the nonradiative exciton lifetime.[5,8] The quantity p_h is defined analogously to n_t [Eq. (4)]:

$$p_h = \beta_h^{-1} e^{-E_h/kT}, \tag{8}$$

where N_v is the valence-band density of states, and β_h is the degeneracy of the hole component of the exciton having binding energy E_h. The recombination kinetics at Zn-O complexes are therefore governed by

$$(n/\tau_{nt})(1-N_t^e/N_t)=(n_t/\tau_{nt})(1-f_0)(N_t^e/N_t)+N_t^e/\tau_t\ , \tag{9}$$

where τ_t is the total lifetime of the N_t^e state. We showed previously[5] that τ_t is given by

$$1/\tau_t=(1-f_0)/\tau_\beta+f_0/\tau_\alpha\ , \tag{10}$$

where τ_β is defined by

$$1/\tau_\beta=1/\tau_{er}+1/\tau_{en}\ . \tag{11}$$

In Eq. (11), τ_{er} is the radiative lifetime of the bare electron trapped at the Zn-O complex due to two processes: pair transitions with distant neutral zinc acceptors and radiative capture of free holes. Lifetime τ_{en} is the nonradiative lifetime of the bare-electron state.[5,8]

The third equation needed to describe the steady-state recombination kinetics is that governing the free electrons:

$$G+(n_t/\tau_{nt})(1-f_0)(N_t^e/N_t)=(n/\tau_{nt})(1-N_t^e/N_t)+(n/\tau_{n0})(1-N_0^0/N_0)+n/\tau_n\ . \tag{12}$$

Equations (2), (9), and (12) determine the steady-state recombination kinetics of the three-path model. The solution of these equations is straightforward. Defining, $\chi_t\equiv N_t^e/N_t$ and $\chi_0\equiv N_0^0/N_0$ as the fraction of electron-filled Zn-O traps and O donors, respectively, we obtain a cubic equation for χ_t:

$$A\chi_t^3+B\chi_t^2+C\chi_t+D=0. \tag{13}$$

The coefficients in Eq. (13) are defined by

$$\begin{aligned}A&=sw(sw-qr),\\ B&=qr[1-q-(1-w)]-sw[1-s(1-2w)]\\ &\quad+gsw(qr-sw),\\ C&=sw[1-s(1-w)]-gsw(qr-2sw),\\ D&=-g(sw)^2.\end{aligned} \tag{14}$$

The dimensionless parameters s, q, r, w and g have special physical significance and are given by

$$s\equiv(1/\tau_{nt})(1/\tau_{nt}+1/\tau_{n0}+1/\tau_n)^{-1}\ , \tag{15}$$

$$q\equiv(1/\tau_{n0})(1/\tau_{nt}+1/\tau_{n0}+1/\tau_n)^{-1}\ , \tag{16}$$

$$r\equiv(N_t/\tau_t)(N_0/\tau_0)^{-1}\ , \tag{17}$$

$$w\equiv(N_t/\tau_t)[(N_t/\tau_t)+(1-f_0)(n_t/\tau_{nt})]^{-1}, \tag{18}$$

$$g\equiv G(N_t/\tau_t)^{-1}. \tag{19}$$

In terms of χ_t the solution for n and χ_0 are

$$n=\chi_t(1-\chi_t)^{-1}N_t(\tau_n/\tau_t)(1-q-s)(ws)^{-1}, \tag{20}$$

$$\chi_0=[1+(ws)(rq)^{-1}(1/\chi_t-1)]^{-1}\ . \tag{21}$$

We now digress briefly from the main development to discuss the physical significance of the parameters defined in Eqs. (15)–(19).

The parameters s and q are the low-level branching ratios for electron capture out of the conduction band and into the Zn-O and O centers, respectively. Thus, s gives the fraction of the total steady-state recombination current which passes through the Zn-O sites. If $s=1$, all recombination proceeds through Zn-O centers, and none through the other two paths. The parameter r gives the relative effectiveness of the Zn-O and O sites in returning trapped electrons to the valence band. The quantity w determines the importance of thermalization of captured electrons out of the Zn-O centers, i.e., w is the branching ratio for electron transfer from the Zn-O trap into the valence band as compared to the total electron transfer to both valence and conduction bands. Finally, g is the volume excitation rate G normalized to the recombination rate N_t/τ_t out of Zn-O complexes.

The general solution to Eq. (13) cannot be expressed in a simple form; we will have need of it only in discussing saturation of the luminescence under high excitation. The low-level values of χ_t and χ_0 can be found by neglecting all but first-order terms in χ_t and g in Eq. (13). This yields

$$\chi_t\approx gsw[1-s(1-w)]^{-1}, \tag{22}$$

$$\chi_0\approx grq[1-s(1-w)]^{-1}. \tag{23}$$

We can calculate the low-level red and infrared luminescence emitted locally in the crystal l_r and l_{ir}, from the expressions

$$l_r=\chi_t(N_t/\tau_r), \tag{24}$$

$$l_{ir}=\chi_0(N_0/\tau_{ir}), \tag{25}$$

where τ_r and τ_{ir} are the radiative lifetimes of the red and infrared emissions, respectively. The lifetime τ_r can be written in terms of previously defined quantities by the relation[5]

$$1/\tau_r\equiv f_0/\tau_{xr}+(1-f_0)/\tau_{er}. \tag{26}$$

Combining Eqs. (22) and (23) with Eqs. (24) and (25) we calculate the low-level internal quantum efficiencies of the red and infrared luminescence η_r^a and η_{ir}^a excited *above* the band gap:

$$\eta_r^a=l_r/G=b_r sw[1-s(1-w)]^{-1}\ , \tag{27}$$

$$\eta_{ir}^a=l_{ir}/G=b_{ir}q[1-s(1-w)]^{-1}\ , \tag{28}$$

where we have defined two more branching ratios $b_r\equiv\tau_t/\tau_r$ and $b_{ir}\equiv\tau_0/\tau_{ir}$, for radiative recombination out of the Zn-O and O centers, respectively. If thermalization is unimportant (i.e., $w=1$), then $\eta_r^a=b_r s$ and $\eta_{ir}^a=b_{ir}^a q$. In this case the above-gap excited efficiencies are products of branching ratios for electron capture out of the conduction band (s and q) and radiative recombination out of the impurity levels (b_r and b_{ir}). If thermalization is im-

portant ($w < 1$), then s and q are coupled and the efficiencies are no longer simple products of branching ratios. If $s = 1$, η_r^a becomes independent of w since all thermalized electrons are eventually recaptured. Thermalization out of Zn-O enhances recombination through oxygen, since fewer minority carriers are effectively captured at Zn-O. For both the red and infrared luminescence, the higher the value of s, the less important is thermalization in its effects on the internal quantum efficiency.

We can also solve for the quantum efficiency of the red and infrared luminescence excited by *below-gap* excitation. (The question of impurity absorption and generation of luminescence by below-gap excitation is discussed in Sec. III.) In this case we take $G = 0$ in Eq. (12) and add the term G_b (the rate of below-gap excitation) to the left-hand side of either Eq. (2) for generation of the infrared luminescence or Eq. (9) for the red luminescence. The below-band-gap–excited infrared efficiency η_{ir}^b is given by

$$\eta_{ir}^b = b_{ir} . \tag{29}$$

Thus, the below-gap efficiency measures directly the b_{ir} branching ratio. For the below-gap excited red efficiency we find that

$$\eta_r^b = b_r w[1 - s(1-w)]^{-1} . \tag{30}$$

Recalling Eq. (27), we see that $\eta_r^a/\eta_r^b = s$, so that the quotient of the two efficiencies is a measure of the s-branching ratio. (In Appendix B we discuss the modifications of this result when excitons are created directly at Zn-O sites by below-gap excitation.)

B. Saturation

When the local generation of minority carriers becomes large enough, the low-level approximations are no longer valid, and the filling fractions χ_t and χ_0 can vary nonlinearly with excitation. Figure 2 gives typical examples of this behavior for $q = 0.01$, $r = 1$, $w = 1$, and variable s. At low excitation the minority carrier recombination divides into three paths with a fraction s going through Zn-O centers, a fraction q going through O centers, and a fraction $1 - s - q$ recombining via the assumed nonsaturable τ_n path. In the examples of Fig. 2 the Zn-O center has been made dominant. Consequently, it fills more rapidly than the O level, approaching its saturated value ($\chi_t = 1$) sublinearly. When this occurs the recombination traffic through Zn-O is diminished with respect to the excitation, and the two remaining paths must furnish a larger fraction of the total recombination. If the O path is comparable to the nonsaturating τ_n path, then it must begin to fill up very rapidly to carry the larger recombination load, thus resulting in a supralinearity when the

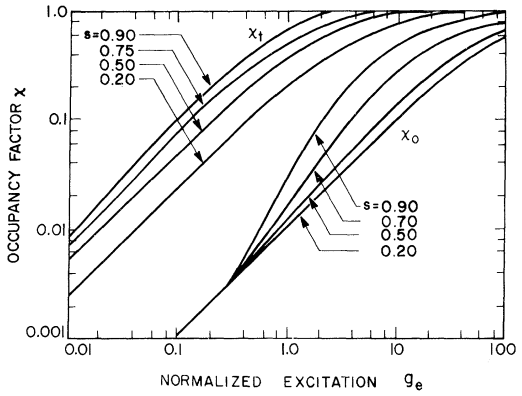

FIG. 2. Variation of the local occupancy factors χ_t and χ_0 at high excitation levels, for several s values, where $q = 0.01$, $r = 1$, and $w = 1$. For large s values, χ_0 increases superlinearly with excitation.

center fills. Conversely, the roles of the two centers may be reversed if q is much larger than s. Alternatively, there is little or no supralinearity if s and q are comparable. Wide variations in the parameter r do not affect the nonlinearities, but simply scale χ_0 through Eq. (21). In the presence of thermalization, i.e., $w < 1$, the effect is approximately the same as reducing s.

In order to determine the dependence of the saturation behavior on material parameters such as lifetimes and capture cross sections, it is convenient to reduce the three-path model to a two-path model in which the oxygen centers are either neglected or lumped together with the τ_n path. In this case we take $q = 0$ and $1/r = 0$ in Eqs. (13) and (14), and obtain a quadratic equation for χ_t. An approximate solution for η_r^a resulting from the solution to this equation is

$$\eta_r^a \approx wsb_r[ws(1+g) + (1-s)]^{-1} . \tag{31}$$

It is convenient to define the condition of saturation as occurring when $wsg_{sat} = (1-s) + ws$, i.e., for G_{sat} defined by

$$G_{sat} = (N_t/\tau_t)[1 + (1/w)(1/s - 1)] . \tag{32}$$

If thermalization is unimportant ($w = 1$), we have from Eqs. (3) and (15)

$$G_{sat} = (v\sigma_{nt}\tau_t\tau_m)^{-1} , \tag{33}$$

where τ_m is the total minority carrier lifetime in the two-path model $1/\tau_m = 1/\tau_{nt} + 1/\tau_n$. If $\tau_m \approx \tau_n$, saturation is seen to be independent of the trap concentration N_t and inversely proportional to the product of lifetimes $\tau_t\tau_m$. If thermalization cannot be neglected, the expression for G_{sat} becomes

$$G_{sat} = (v\sigma_{nt}\tau_t\tau_m)^{-1} + (1/\tau_n)(1 - f_0)N_c\beta_t e^{-E_t/kT} , \tag{34}$$

where we have used Eqs. (3), (4), (15), and (18). Thermalization thus acts to delay the onset of saturation to a degree determined by the strength of the nonsaturable path $1/\tau_n$.

C. Nonlocal Solutions

The local saturation behavior can be observed only in the case of excitation uniform throughout the crystal. In practice, the excitation is highly nonuniform owing to the absorption process. An additional complicating feature of laser excitation is the Gaussian beam shape. For laser photoexcitation, the number of electron-hole pairs generated per unit volume per second can be expressed at any point (ρ, z) within the crystal as

$$G = \alpha_e I_e \exp(-\alpha_e z - 2\rho^2/\rho_0^2). \tag{35}$$

Here I_e is the laser excitation flux *within the crystal* at the surface in units of photons $cm^{-2}\,sec^{-1}$, ρ is the radial coordinate normal to the optical axis of the beam, ρ_0 is the Gaussian beam half-width, and α_e is the absorption coefficient. The local filling fractions χ_t and χ_0 can be found in terms of $g = G/(N_t/\tau_t)$ for any excitation level from Eqs. (13) and (21). The total luminescence L emitted from the crystal is then

$$\mathcal{L}_r = (N_t/\tau_r)\int_V \chi_t(\rho, z)\, d^3r, \tag{36}$$

$$\mathcal{L}_{ir} = (N_0/\tau_{ir})\int_V \chi_0(\rho, z)\, d^3r, \tag{37}$$

where V is the volume of the crystal. Defining $g_e \equiv \alpha_e I_e/(N_t/\tau_t)$, it can be shown for an infinite half-plane that

$$\mathcal{L}_r(g_e) = (N_t/\tau_r)(\pi\rho_0^2/2\alpha_e)\int_0^1 du \int_0^1 dv\, \chi_t(uvg_e)/uv, \tag{38}$$

with a similar expression for $\mathcal{L}_{ir}(g_e)$ obtained by replacing N_t/τ_r by N_0/τ_{ir} and χ_t by χ_0. The integrands are functions of the product uvg_e, and the complicated nature of the expressions involved makes it difficult to express $\mathcal{L}_r$ and $\mathcal{L}_{ir}$ in closed form.

For comparison of the model calculations with photoluminescence saturation experiments, both the integrand and integral are calculated numerically using a computer. Each set of the parameters (s, q, r, w) results in two theoretical saturation curves $\mathcal{L}_r(g_e)$ and $\mathcal{L}_{ir}(g_e)$, which can be compared with the experimental measurements to obtain the important G_{sat} parameter (see Sec. V). In Fig. 3 we show the normalized luminescence $L_r \equiv \mathcal{L}_r(\tau_r/N_t) \times (2\alpha_e/\pi\rho_0^2)$ for $q = 0.01$, $r = 1$, $w = 1$ with s as a variable parameter. For s not close to unity we find that L_r is essentially independent of r. It should be noted that the inclusion of spatial effects makes the saturation curve vary much more slowly than in the local case (compare Figs. 2 and 3). For electroluminescent saturation[7] the luminescence varies

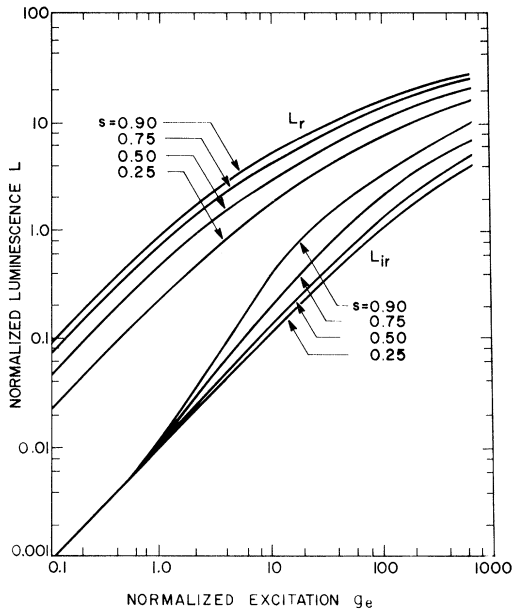

FIG. 3. The nonlocal normalized luminescence L_r and L_{ir} corresponding to the values used in Fig. 2.

logarithmically with excitation due to the one-dimensional exponential falloff of the injection. The additional Gaussian radial falloff of the laser excitation in photoluminescence experiments gives rise to a log-squared behavior. We point out that our analysis neglects diffusion of minority carriers, but gives the complete three-dimensional spatial dependence[19] when $1/\alpha_e$ and ρ_0 are larger than the diffusion length.

D. Determination of Deep Concentrations

We now wish to show, on the basis of the previous discussion, that the branching ratios s and q and the concentrations N_t and N_0 can be determined from a series of five measurements: (i) impurity absorption below the band gap, (ii) internal photoluminescence quantum efficiency for below-band-gap excitation, (iii) internal photoluminescence quantum efficiency for above-band-gap excitation, (iv) photoluminescence saturation, and (v) decay time of luminescence.

A typical optical absorption curve for GaP(Zn, O) is shown in Fig. 4. Two absorption bands are observed for excitation below the band gap.[22] Excitation at room temperature near the peak of the lower energy band ($h\nu \approx 1.35$ eV) results in infrared luminescence characteristic of recombination at oxygen sites. This implies that the ionized O level in the p-type material is photoneutralized by electrons elevated from the valence band by the exciting radiation. Likewise, when the excitation lies in the higher energy band ($h\nu \approx 1.8$ eV) red luminescence

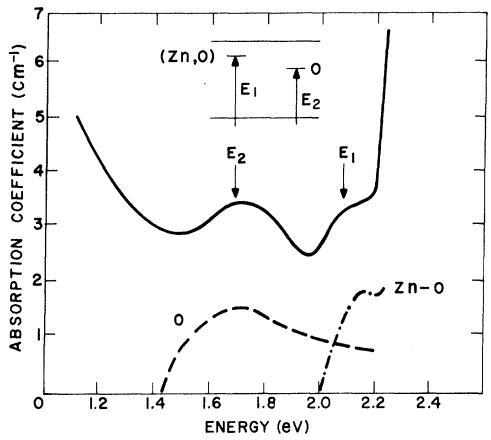

FIG. 4. A typical absorption spectrum at 300 °K for GaP(Zn, O) doped with 0.07 mol% Zn, 0.02 mol% Ga_2O_3. The maxima at energies E_1 and E_2 correspond to absorption by Zn-O and O centers, respectively, as indicated in the inset. Also shown are the shapes of the individual impurity absorption curves as determined from photoluminescence excitation measurements. These curves are in relative units and do not represent the partial absorption coefficients of the two processes.

characteristic of radiative recombination at Zn-O centers is observed. In this case the absorbed radiation can result in the creation of both bound-exciton and bare-electron states at Zn-O sites. (Elaboration of this point is made in Appendix B.) It is possible to measure the efficiencies of the below-gap excited red and infrared luminescence η_r^b and η_{ir}^b if the amount of absorbed excitation can be calculated. This requires determining the absorption coefficients for the two bands, i.e., making measurement (i). Measurements (ii) and (iii) then determine s through the relation [recall Eqs. (27) and (30)] $\eta_r^a/\eta_r^b = s$. With s determined, the ratio N_t/τ_t can be found from G_{sat} [measurement (iv)] if w is known [see Eq. (32)]. The quantity w can be calculated from Eq. (18) if the trap level E_t, the cross section σ_{nt}, and the lifetime τ_t are known. In Sec. V we show (for $T = 300\,^\circ$K) that for GaP(Zn, O) $E_t \approx 0.230$ eV and $\sigma_{nt} = 2.0\times10^{-16}$ cm^2. In most cases we also have $f_0 \ll 1$. Thus, it τ_t can be determined, w is obtained from Eq. (18), and N_t is determined from Eq. (32). We showed in a previous paper[5] that the total lifetime τ_t is related to the luminescence decay time $\tau_{1/e}$ in a simple way under the conditions

$$(p_0+p_h) \gg N_t\tau_{pt}/\tau_\alpha\,, \qquad (p_0+p_h) \gg N_t\tau_{pt}(1/\tau_\beta + n_t/N_t\,\tau_{nt}). \tag{39}$$

Under these conditions, with $s \ll 1$ (a practically important limit) we obtain from Eqs. (15), (20), and (32) of Ref. 5 the result

$$1/\tau_{1/e} = 1/\tau_t + (1-f_0)n_t/N_t\,\tau_{nt}\,. \tag{40}$$

Equation (40) shows that $\tau_{1/e}$ is *shortened* with respect to τ_t by thermalization and subsequent recombination through the nonsaturable path. (The difference between $\tau_{1/e}$ and τ_t was illustrated in Fig. 3 of Ref. 5.) Clearly, if $s = 1$, thermalization can have very little effect on the decay time, since all thermalized carriers are ultimately recaptured by the Zn-O centers during the course of the decay. (Our model neglects the effects of trapping centers in lengthening the decay time over τ_t even if $s = 1$.) Consequently, in the low-excitation limit we can include the effect of s on the decay time by multiplying the second term in Eq. (40) by $(1-s)$. Thus, the generalized decay time under the conditions of Eq. (39) is given by[23]

$$1/\tau_{1/e} = 1/\tau_t + (1-s)(1-f_0)n_t/N_t\,\tau_{nt}\,. \tag{41}$$

Since all parameters in the second term of Eq. (41) are determined as described earlier, τ_t is immediately obtained from the decay time [measurement (v)]. [Also note $G_{sat} = (v\sigma_{nt}\,\tau_m\tau_{1/e})^{-1}$.]

For oxygen we determine q from efficiency data through Eqs. (28) and (29) with s and w obtained as described above. The dependence of the infrared luminescence saturation on material parameters can be found from Eqs. (21) and (31). We find that the infrared luminescence saturates at a value $G_{sat} = (N_0/\tau_0 q)[ws + (1-s)]$. In the absence of thermalization out of oxygen the decay time of the infrared luminescence is just the total lifetime τ_0. Hence, N_0 is determined from efficiency, saturation, and decay-time measurements using the above relation.

III. MEASUREMENT OF INTERNAL QUANTUM EFFICIENCY

Measurement of the internal quantum efficiencies of the red and infrared luminescence is essential in determining the concentrations of Zn-O complexes (N_t) and oxygen donors (N_0) as well as the parameters s and q. In Appendix C we show that the internal efficiencies can be determined by measurement of the surface radiance on samples with parallel plane geometry. The method considered is similar to that used by Vilms and Spicer[16] for near-band-gap luminescence in GaAs. Since the absorption coefficients for the red and infrared luminescence in GaP are relatively small, we include in our analysis the added complication of multiple internal reflections of the luminescence. In addition, we distinguish between situations where the exciting photons have energies below or above the band gap.

A. Above-Band-Gap Excitation

The geometry used in above-band-gap radiance measurements is shown in Fig. 5. The semi-infi-

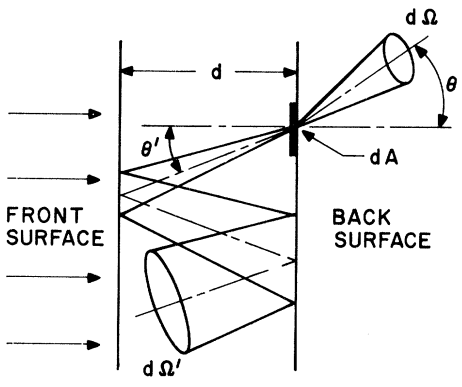

FIG. 5. Geometry used in above-gap radiance measurement. Luminescence falling in the receiver cone $d\Omega$ originates from the internal solid angle $d\Omega'$ as discussed in the text.

nite sample of thickness d and index of refraction n lies normal to the z axis. Uniform excitation incident on the front surface ($z=0$) generates the luminescence which is observed on the back surface ($z=d$). To calculate the radiance $\mathcal{R}_\theta$ (in units of photons/sec cm^2 sr) we consider the external luminescence coming from a small area dA on the back surface and lying in a small solid angle $d\Omega$ whose axis makes an angle θ with the sample normal. As shown in Fig. 5, the external luminescence has its origin in the internal solid angle $d\Omega' = [\cos(\theta)/n^2\cos\theta']\,d\Omega$ which includes the effects of multiple reflections from the front and back specular surfaces. We show in Appendix C that in the limit where surface recombination does not dominate, the radiance $\mathcal{R}_\theta$ is given by [Eq. (C6)]

$$\mathcal{R}_\theta = \frac{(1-R_a)}{4\pi n^2}\left(\frac{\cos\theta}{\cos\theta'}\right) I_a \int_{E_1}^{E_2} dE\,(1-R_{\theta'}^2) \times \left(\frac{\exp(-\alpha d/\cos\theta')}{1-R_{\theta'}^2\exp(-2\alpha d/\cos\theta')}\right)\eta^a(E). \quad (42)$$

Here R_a and I_a are, respectively, the reflection coefficient and intensity of the above-band-gap excitation; $R_{\theta'}$ and α are, respectively, the reflection coefficient and absorption coefficient of the radiation emitted at photon energy E in the band (E_1, E_2); n is the refractive index of the medium; and $\eta^a(E)$ is the incremental internal quantum efficiency at energy E.

To determine the radiance experimentally a substitutional technique is used. The photon flux through dA measured by the detector is

$$\Phi = 2\pi\int_0^{\theta_0} \mathcal{R}_\theta \sin\theta\, d\theta\,, \quad (43)$$

where θ_0 is the maximum angle subtended by the detector input cone. For small θ_0 we can approximate Eq. (43) by

$$\Phi \approx \pi\theta_0^2\mathcal{R}_0\,, \quad (44)$$

where $\mathcal{R}_0$ is the radiance measured normal to the sample surface. If a standard radiance source $\mathcal{R}_S$ is substituted for $\mathcal{R}_0$ in the same geometry, then we measure $\Phi_S = \pi\theta_0^2\mathcal{R}_S$ so that $\mathcal{R}_0 = \mathcal{R}_S(\Phi/\Phi_S)$. The total internal quantum efficiency for the luminescent band

$$\eta^a \equiv \int_{E_1}^{E_2}\eta^a(E)\,dE$$

may then be obtained from Eq. (42) by taking $\theta=\theta'=0$ and using average values (with respect to E) for α and the reflection coefficient.

B. Below-Band-Gap Excitation

When the energies of the exciting photons lie below the band gap no free electrons are created, and hence minority carrier diffusion is absent. In this case the spatial dependence of the luminescence is just that of the excitation $G_b(z)$, and the constant of proportionality is the below-gap internal efficiency, i.e.,

$$l(z,E) = \eta^b(E)G_b(z). \quad (45)$$

For this situation the absorption coefficient α_b of the below-gap excitation is low and multiple reflections become important. It is easy to show that $G_b(z)$ has the form

$$G_b(z) = (1-R_b)\alpha_b I_b(e^{-\alpha_b z} + R_b e^{\alpha_b(z-2d)}) \times (1-R_b^2 e^{-2\alpha_b d})^{-1}, \quad (46)$$

where R_b and I_b are the reflection coefficient and incident intensity, respectively, of the excitation. It is a simple matter to use Eqs. (45) and (46) to derive an equation for this case analogous to Eq. (42). From an experimental point of view, however, it is not practical to measure the radiance using the geometry of Fig. 5, since the transmitted excitation cannot be wholly removed by filtering. An alternative geometry used for below-band-gap excitation is shown in Fig. 6. In the arrangement shown, the sample acts as a point-source emitter, since its dimensions are small compared with the distance to the detector. The signal measured by the detector is not proportional to the radiance of a small area of the sample surface as in the previous case, but is rather a measure of the total external quantum efficiency. Since the sample behaves as a point source, the detected power is independent of the spatial distribution of the luminescence within the crystal and is simply proportional to the internal efficiency and the absorbed excitation. Thus, the ratio of the signals measured for below- and above-band-gap excitation is given by

$$\frac{\Phi_b}{\Phi_a} = \left(\frac{\eta^b}{\eta^a}\right) \int_0^d G_b(z)\,dz \Big/ \int_0^d dz\, \frac{n(z)}{\tau_m} \quad . \tag{47}$$

Measurement of this ratio in the geometry of Fig. 6 determines η^b in terms of η^a, and the latter quantity is determined by measurement of $\mathcal{R}_0$ in the geometry of Fig. 5.

It is important to note that the absorption coefficient α_b used in Eq. (46) is *not* the total absorption coefficient as determined by a transmission measurement. Rather, it is the partial coefficient due to the creation of N_t^e-type states in the case of the Zn-O complex, or N_0^0-type states for the oxygen donor. To obtain α_b we must separate the total absorption coefficient into its various components. This will be discussed further in Sec. V.

IV. SPECTRAL SHAPES OF RED AND INFRARED LUMINESCENCE BANDS

To determine the over-all internal quantum efficiency for recombination at Zn-O or O centers it is necessary to properly perform the integration over the emission bands associated with recombination at these centers [see Eq. (42)]. Thus it is important to accurately determine the spectral shapes of the luminescence associated with Zn-O and O centers. This is a difficult problem at room temperature because of the considerable overlap between the two emission bands. As shown in Fig. 7 the two bands, which are distinctly separate at lower temperatures, become merged above 200 °K. The overlap results, to a large degree, from the unusual variation with temperature of the infrared emission. While the position of the maximum of the red band follows the band-gap shift with temperature, the maximum of the infrared band *increases* with

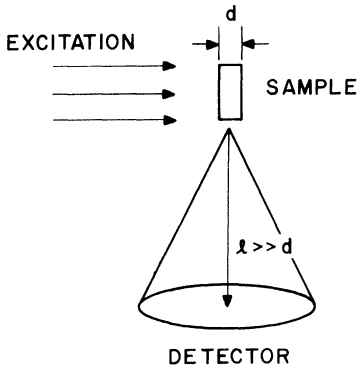

FIG. 6. Geometry used in measuring the below-gap internal quantum efficiency. The luminescence is detected at right angles to the incident beam direction to minimize interference by the excitation. The distance between sample and detector is large compared with the sample dimensions so that it acts as a point-source emitter.

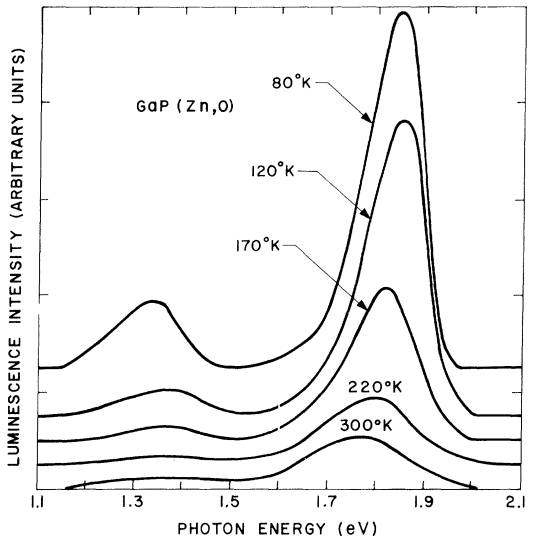

FIG. 7. Temperature dependence of photoluminescence spectra from as-grown GaP(Zn, O) doped with 0.07 mol% Zn and 0.02 mol% Ga_2O_3. The zero of each curve has been shifted for clarity. Each curve has been corrected for grating and detector response.

increasing temperature above 80 °K.[2] In addition, both bands show broadening on both the low- and high-energy sides of the peaks, due to increased phonon cooperation at the higher temperatures.

The spectral shape of the infrared luminescence due only to recombination at oxygen donors can be determined by exciting the crystal with appropriate below-band-gap radiation. As seen from the impurity absorption spectrum shown in Fig. 4, the infrared luminescence can be preferentially excited by radiation at $h\nu \approx 1.85$ eV. The resulting room-temperature emission is shown in Fig. 8(a). At room temperature the infrared band has a high-energy threshold of 1.63 eV, peaks at 1.36 eV, and exhibits a very long low-energy tail extending to 0.89 eV.

The difficulty in achieving a unique separation of the two luminescence bands arises from the possibility that the red emission also has a long low-energy tail that extends appreciably into the spectral region where the infrared luminescence peaks.[17] The red luminescence cannot be excited preferentially because the absorption band for direct photoexcitation of the Zn-O level is overlapped entirely by the absorption band for oxygen (see Fig. 4). It is possible, however, to separate the two radiative processes by means of time-decay measurements, since the excitonic red emission decays much more rapidly than the infrared pair emission. By determining the relative strengths of the fast and slow decaying components of the above-gap excited emis-

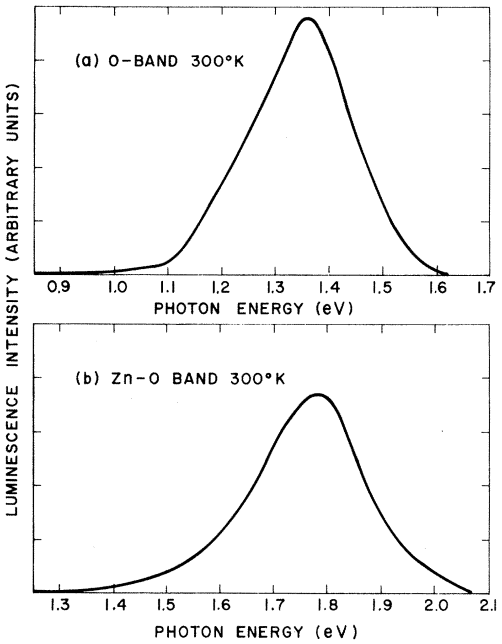

FIG. 8. Room-temperature spectral shapes of radiative recombination originating at (a) oxygen donors and (b) zinc-oxygen complexes in GaP(Zn, O).

sion in the range where the bands overlap ($1.4 \leq h\nu < 1.5$ eV), it is possible[18] to deduce what fraction of the total luminescence in this spectral range results from recombination at oxygen. By subtracting this fraction of the infrared band from the total emission we obtain the spectral shape of the Zn-O recombination band. This is shown in Fig. 8(b). A comparison of Figs. 8(a) and 8(b) reveals that the Zn-O recombination does in fact have a long tail on the low-energy side which extends well into the infrared emission region. The other features of the red band shown in Fig. 8(b), i.e., the peak position and high-energy threshold, are in essential agreement with previous work.[24]

V. RESULTS

In this section we consider several different kinds of experimental information concerning GaP(Zn, O) and present a semiquantitative self-consistent interpretation of the results in terms of the three-path recombination model formulated in Sec. II. In particular, we wish to evaluate the following data for the red luminescence: (i) temperature dependence of $\tau_{1/e}$, (ii) temperature dependence of η_r^b, (iii) Zn concentration dependence of $\tau_{1/e}$ measured at 300 °K, and (iv) Zn concentration dependence of η_r^a measured at 300 °K. For each of these categories we wish to explain the absolute as well as the relative magnitudes of the parameters. The interpretation of the above experiments requires some minor modifications of our earlier work[5] in which we fitted the temperature dependence of $\tau_{1/e}$. In achieving that fit the magnitude (C_{pt}) and temperature variation (m) of the hole capture cross section σ_{pt} were varied, where

$$\sigma_{pt} = C_{pt} T^{-m}. \tag{48}$$

All other parameters entering into the calculation, such as the radiative and nonradiative lifetimes τ_{xr}, τ_{xn}, τ_{er}, and τ_{en}, were fixed at their known values or at values obtained from reasonable theoretical estimates. In particular, the nonradiative lifetimes τ_{xn} and τ_{en} due to the Auger processes were taken to be of the form[8]

$$1/\tau_{xn} = Bp, \tag{49}$$

$$1/\tau_{en} = Cp^2. \tag{50}$$

The ratio B/C was then selected to agree with its calculated value,[8] and B was adjusted to give agreement with the measured value of η_r^b in crystals for which $N_A - N_D \approx 1\times10^{18}$ cm^{-3}, i.e., $\eta_r^b \approx 0.10$. (The experimental determination of η_r^b is discussed below.)

In the present work we show that the temperature dependence of σ_{pt} is determined almost entirely from plasma screening of the Coulomb binding potential by free holes. In addition, we include the effects of screening on the excitonic hole binding energy E_h, the excitonic Auger coefficient B, and the excitonic radiative lifetime τ_{xr}. In order to obtain agreement between the recombination model with screening included and the four categories of experimental data outlined above, we have at our disposal four adjustable parameters, i.e., B, C, σ_{nt}, and E_t. We use a self-consistent iterative approach in which the previous results[5] for B and C, determined from the temperature dependence of $\tau_{1/e}$ (which is essentially independent of σ_{nt} and E_t below 300 °K), are used as starting values in fitting σ_{nt} and E_t to the remaining three categories of data [(ii)–(iv)]. The iteration proceeds through slight adjustments of the parameters until self-consistency is achieved. It should be noted that there is, on the average, one adjustable parameter for each independent set of experimental data. It is possible, therefore, to find values of the parameters that give good fits to the temperature dependence of $\tau_{1/e}$ without correctly explaining its doping dependence. Likewise, regions of parameter space that successfully fit the doping dependence of $\tau_{1/e}$ do not necessarily give fits to the doping dependence of η_r^a. In our self-consistent approach, the final values of the parameters are therefore a compromise between the various sets of data to be explained. Within the constraints of the model calculation, the final self-consistent fit is unique.

In achieving a fit we determine E_t and σ_{nt}, the two quantities needed to calculate w [see Eq. (18)]. With w specified, the five measurements outlined in Sec. IID can be used in determining the concentrations of Zn-O and O centers. In the latter part of this section we report luminescence efficiency, saturation, and decay-time data from which we determine the Zn-O and O concentrations in several solution-grown crystals. We also consider the effects of annealing in changing the Zn-O and O concentrations, and as a result, the measured time-decay and quantum efficiencies.

A. Screening Effects

The effects of free-hole screening on recombination at Zn-O complexes have been treated in detail elsewhere.[8] It has been shown[25] that as a result of screening, the binding energy E_h of a hole to a charged complex decreases with increasing hole concentration according to

$$E_h = E_h^0 - 10^{-8} p_0^{1/3} \text{ eV}, \tag{51}$$

where E_h^0 is the low-concentration binding energy ($E_h^0 = 36$ meV for the Zn-O center).[3] The excitonic Auger coefficient B is likewise reduced by screening[8]:

$$B = B_0 (E_h / E_h^0)^{5/2}, \tag{52}$$

where B_0 is a constant. As shown in Appendix D, the radiative excitonic lifetime τ_{xr} is increased by screening through the relation[26]

$$\tau_{xr} = \tau_{xr}^0 (E_h^0 / E_h)^{5/2}, \tag{53}$$

where τ_{xr}^0 is the low-temperature intrinsic exciton lifetime ($\tau_{xr}^0 = 0.1$ μsec for the Zn-O center in GaP).[3,4] Finally, the capture cross section σ_{pt} is reduced by screening from its unscreened value σ_{pt}^0, i.e.,

$$\sigma_{pt} = \sigma_{pt}^0 S, \tag{54}$$

where in the Debye limit the screening factor S is given by[8]

$$S \equiv [1 + (2\pi e^2 \hbar^2 p_0 / m_v^* \epsilon k T E_h)^{1/2}]^{-8}. \tag{55}$$

In Eq. (55) m_v^* is the valence-band effective mass, and ϵ is the dielectric constant ($\epsilon = 11.1$ for GaP).[27]

We can account for practically all of the temperature dependence of σ_{pt} reported previously[5] (i.e., $\sigma_{pt} = 3.6 \times 10^{-16}\ T^{-1}$ cm^2 at $N_A - N_D \approx 10^{18}$ cm^{-3}) by assuming that σ_{pt}^0 in Eq. (54) is a constant. In Fig. 9 we plot S versus T for two acceptor concentrations, and for comparison we also plot $\sigma_{pt} = 3.6 \times 10^{-16}\ T^{-1}$. Above 125 °K both S and σ_{pt} are essentially constant. In the range 20 °K $\leq T \leq$ 125 °K the decrease in S and σ_{pt} with increasing temperature are approximately equal, although the T^{-1} dependence falls off somewhat more rapidly. Because of the similarity in the calculated temperature dependence of S and the experimentally determined temperature dependence of σ_{pt}, we shall assume that the entire functional dependence of σ_{pt} on p_0 and T above 20 °K is determined by S, i.e., we take σ_{pt}^0 in Eq. (54) to be a constant: $\sigma_{pt}^0 = 2.1 \times 10^{-17}$ cm^2. We conclude, therefore, that the room-temperature value of σ_{pt} in heavily Zn-doped material ($\sigma_{pt} \approx 10^{-18}$ cm^2) can be explained on the basis of screening, which results in an almost 20-fold decrease in σ_{pt} as the holes become thermalized. In lightly Zn-doped material S is less sensitive to temperature (see Fig. 8) and consequently σ_{pt} is almost an order of magnitude larger at room temperature than in heavily doped crystals. In the model calculations described below, screening effects are included by means of Eqs. (51)–(55).

B. Determination of Model Parameters

Using the iterative self-consistent method outlined previously, we have adjusted B_0, C, σ_{nt}, and E_t to achieve agreement between the model calculation and the following experimental data: (i) $\tau_{1/e}$ versus T as determined by Cuthbert *et al.*[4] for $N_A - N_D \approx 10^{18}$ cm^{-3} (see Fig. 2 of Ref. 5); (ii) $\eta_\gamma^b(220\ ^\circ\text{K})/\eta_\gamma^b(270\ ^\circ\text{K}) = 4.1$ for $N_A - N_D = 2 \times 10^{17}$ cm^{-3} (see Fig. 10); (iii) $\eta_\gamma^b(300\ ^\circ\text{K}) = 10\%$ for $N_A - N_D = 2 \times 10^{18}$ cm^{-3} (see Sec. V C); (iv) $\tau_{1/e}$ versus N_A

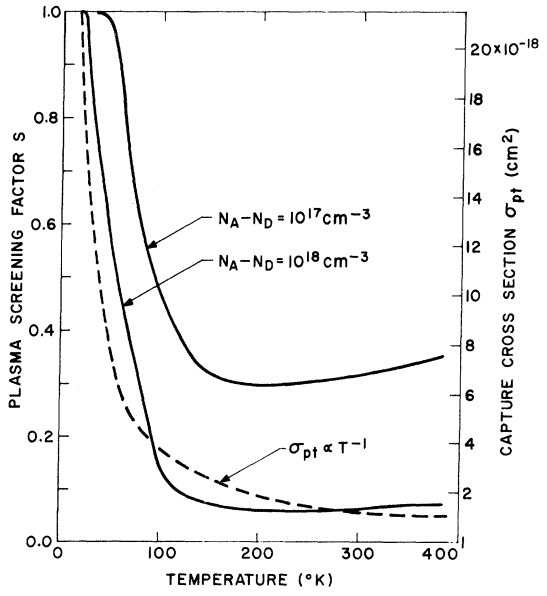

FIG. 9. Temperature dependence of the plasma screening factor S for two net acceptor concentrations. The dashed curve shows the temperature dependence of the capture cross section $\sigma_{pt} = 3.6 \times 10^{-16}\ T^{-1}$ cm^2.

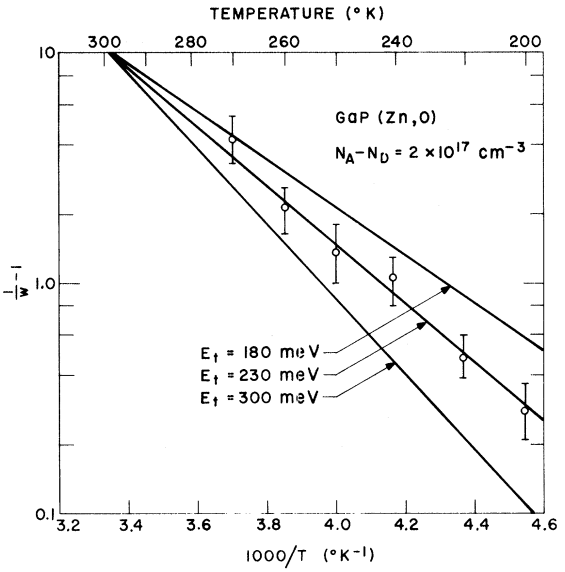

FIG. 10. Calculated plots of $1/w - 1$ [the right-hand side of Eq. (56)] for three values of the binding energy E_t. The open circles have been calculated, using the left-hand side of Eq. (56) with $b_r = 0.5$, from below-gap red efficiency data for a crystal with $N_A - N_D \approx 2 \times 10^{17}$ cm^{-3}.

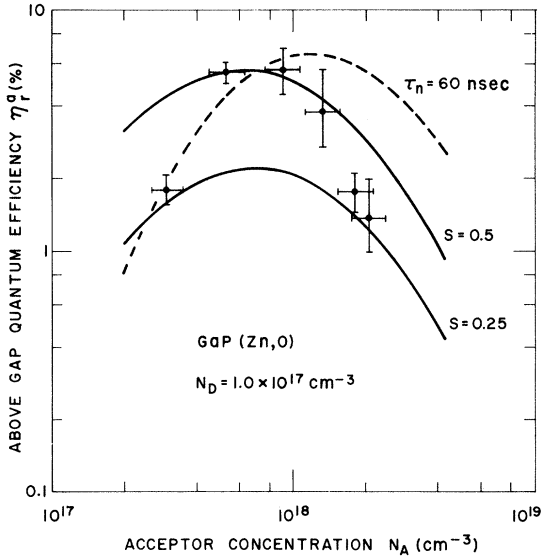

FIG. 12. Above-gap internal quantum efficiency of the red luminescence as a function of acceptor concentration assuming $N_D = 1 \times 10^{17}$ cm^{-3}. The curves were calculated for two values of constant s and one value of constant τ_n using the values of parameters given in Table I. The $\tau_n = 60$-nsec curve assumes 1% of the acceptors form Zn-O complexes. The data points represent the average of five crystals measured for each value of N_A.

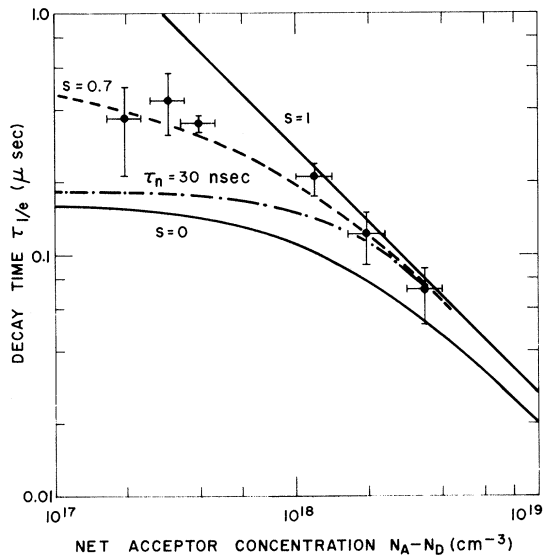

FIG. 11. Red luminescence decay time as a function of net acceptor concentration calculated for three values of constant s and one value of constant τ_n using the values of parameters given in Table I. The $s = 1$ curve corresponds to the total lifetime τ_t [see Eq. (41)]. The $\tau_n = 30$-nsec curve assumes 1% of the acceptors form Zn-O complexes (Tables II and III). The data points are from Ref. 28.

$- N_D$ for $T = 300$ °K (see Fig. 11); (v) η_r^a versus $N_A - N_D$ for $T = 300$ °K (see Fig. 12). A best fit to these data is obtained for $B_0 = 5.0 \times 10^{-11}$ cm^{-3} sec^{-1}, $C = 2.5 \times 10^{-30}$ cm^{-6} sec^{-1}, $\sigma_{nt} = 2.0 \times 10^{-16}$ cm^2, and $E_t = 0.23$ eV. A summary of the parameters used in making the model calculations is given in Table I.

The parameters B_0 and C are determined primarily by the fit to the temperature dependence of the decay time. In varying these parameters from the values used in our previous calculation[5] we have maintained essential agreement between the calculated and experimental values of $\tau_{1/e}$ versus T as given in Fig. 2 of Ref. 5. In order to achieve agreement in the range $200 \leq T \leq 300$ °K it is necessary to calculate $\tau_{1/e}$ from Eq. (41), using a value of $s \approx 0.6$. As will be shown below (see Tables II and III), this is a reasonable choice for solution-grown crystals of GaP(Zn, O) in which $N_A - N_D \approx 10^{18}$ cm^{-3}.

The parameters σ_{nt} and E_t are most sensitive to the fit of the temperature dependence of the below-gap efficiency η_r^b. Combining Eqs. (18) and (30), we find that

$$(1 - s)^{-1}(b_r/\eta_r^b - 1) = v\sigma_{nt}N_c\tau_t\beta_t e^{-E_t/kT}. \quad (56)$$

From this result we expect η_r^b to quench rapidly with temperature when the right-hand side of Eq.

TABLE I. Parameters used in performing model calculations for GaP(Zn, O).

Zn-O electron trap level (300 °K)	$E_t = 0.230$ eV
Exciton hole ionization energy	$E_h^0 = 0.036$ eV
Zn acceptor ionization energy	$E_A = 0.064 - 3\times10^{-8} N_A^{1/3}$ eV
Exciton radiative lifetime	$\tau_{xr}^0 = 0.100$ μsec
Zn-O electron trap capture cross section	$\sigma_{nt} = 2.0\times10^{-16}$ cm^2
Zn-O hole trap capture cross section	$\sigma_{pt} = 3.6\times10^{-16}\, T^{-1}$ cm^2
Auger B coefficient [Eqs. (49) and (52)]	$B_0 = 5\times10^{-11}$ cm^3/sec
Auger C coefficient [Eq. (52)]	$C = 2.5\times10^{-30}$ cm^6/sec
Valence-band effective mass	$m_v^* = 0.92\times$(free-electron mass)
Conduction-band effective mass	$m_c^* = 0.35\times$(free-electron mass)
Zn-O bare-electron degeneracy factor	$\beta_t^{-1} = 2$
Zn-O hole degeneracy factor	$\beta_h = 2$

(56) is greater than unity. This thermal quenching of η_r^b will occur below room temperature for crystals with a low net acceptor concentration (i.e., a low value of p), since in this case τ_t is lengthened by the increased Auger lifetimes [Eqs. (49) and (50)]. We have measured η_r^b versus T in crystals for which $N_A - N_D \approx 2\times10^{17}$ cm^{-3} and find that the efficiency decreases by approximately a factor of 4 as the temperature is raised from 220 to 270 °K. We have used these data in plotting the left-hand side of Eq. (56) in Fig. 10 and have made use of the fact that for $N_A - N_D \approx 2\times10^{17}$ cm^{-3} b_r is essentially temperature independent in the range 220–270 °K, i.e., $b_r = 0.5$ (see Fig. 13). In comparing the model calculation with the experimental points in Fig. 10, we have constrained the calculated curves to give $(1/w - 1) = 10.1$ at 300 °K in order to preserve the self-consistent fits to the remaining categories of data taken at room temperature [i.e., categories (ii), (iv), and (v) listed above]. As shown in Fig. 10, the best fit under this constraint is achieved for $E_t = 0.23 \pm 0.02$ eV. The corresponding value for the cross section is $\sigma_{nt} = 2^{+2.0}_{-0.7}\times10^{-16}$ cm^2.

The calculated dependence of $\tau_{1/e}$ with doping is shown in Fig. 11. The decay time at any value of $N_A - N_D$ is required to lie between the lower ($s = 0$) and upper ($s = 1$) curves. The upper ($s = 1$) curve gives the doping dependence of the total lifetime τ_t [see Eq. (41)]. It follows a power-law dependence with exponent slightly greater than unity, resulting from the combination of linear and quadratic Auger lifetimes τ_{xn} and τ_{en} [Eqs. (49) and (50)]. The $s = 0$ curve displays the greater relative importance of thermalization at lower doping. For low values of $N_A - N_D$ the total lifetime τ_t of trapped electrons on Zn-O complexes becomes long, since with both, radiative and nonradiative lifetimes are lengthened. Thus, an electron can, in effect, wait sufficiently long in a bare-electron state for thermalization into the conduction band to occur. This is reflected in the lower value of the branching ratio w at low $N_A - N_D$ (see Fig. 13). The data shown in Fig. 11 were obtained by Hackett and Bhargava[28] on annealed crystals (600 °C for 5 h) of GaP(Zn, O). We obtain an excellent fit to their results by assuming a constant value of $s = 0.7$ over the full range of $N_A - N_D$. For comparison, a plot of $\tau_{1/e}$ versus $N_A - N_D$ assuming a constant $\tau_n = 30$ nsec is also shown. The constant τ_n curve has been calculated assuming that the Zn-O complex concentration is proportional to N_A.[14] The constancy of s with $N_A - N_D$ implied by the data suggests that the shunt-path lifetime τ_n is inversely proportional to the Zn concentration[29] [see Eq. (15)].

The constancy of s with doping is also suggested by the above-band-gap efficiency data shown in Fig. 12. At each concentration N_A the internal efficiency η_r^a was measured for approximately five unannealed solution-grown[20] crystals. The error bars indicate the spread in results. As with the time-decay data, the measured efficiencies are better fit by constant s curves rather than constant τ_n curves. The calculated plot for $\tau_n = 60$ nsec implies that higher quantum efficiencies are possible if the τ_n path can be controlled with doping. The rapid quenching of the efficiency at high Zn concentrations results from a simultaneous shortening of τ_t (Fig. 11) and a decrease in f_0 which quenches b_r as the hole concentration is raised. The quenching of b_r with doping is only partially offset by an

TABLE II. Results of the five measurements discussed in Sec. II D for crystal MS 80725-0.

	η_r^a (%)	η_{ir}^a (%)	η_r^b (%)	η_{ir}^b (%)	s	q	N_t(cm^{-3})	N_0(cm^{-3})	σ_{n0}(cm^2)	τ_n(nsec)
As grown	5.4	1.8	7.1	0.39	0.76	0.027	3.9×10^{16}	2.5×10^{17}	5.5×10^{-19}	46
			9.5	0.13	0.57	0.098	2.9×10^{16}	7.6×10^{17}	6.5×10^{-19}	30
Annealed[a]	5.0	0.77	6.9	0.39	0.72	0.012	7.5×10^{16}	1.1×10^{17}	1.1×10^{-18}	18
			9.2	0.13	0.54	0.043	4.7×10^{16}	3.1×10^{17}	1.2×10^{-18}	14

[a]Annealing was performed at 600 °C for 5 h.

TABLE III. Results of model calculation combined with efficiency and saturation data for several solution-grown GaP crystals grown from a melt containing 0.07 mol% Zn and 0.02 mol% Ga_2O_3.

Crystal	η_r^a (%)	η_{ir}^a (%)	η_{ir}^b (%) [a]	s	q [a]	N_t(cm^{-3})	N_0(cm^{-3}) [a]	σ_{no}(cm^2)	τ_n(nsec) [a]
As grown									
MS 80725-1	2.5	0.45	{0.13 0.39}	0.34	{0.029 0.009}	2.5×10^{16}	{1.2×10^{17} 3.8×10^{16}}	1.4×10^{-18}	{11 10}
MS 80305-0	3.5	0.75	{0.13 0.39}	0.44	{0.045 0.015}	1.4×10^{16}	{2.2×10^{17} 6.8×10^{16}}	6.5×10^{-19}	{31 29}
MS 80725-13	4.2	1.2	{0.13 0.39}	0.50	{0.069 0.022}	1.2×10^{16}	{2.0×10^{17} 6.4×10^{16}}	8.3×10^{-19}	{48 44}
MS 80725-7	6.1	1.8	{0.13 0.39}	0.65	{0.092 0.029}	1.7×10^{16}	{1.2×10^{17} 3.8×10^{16}}	8.5×10^{-19}	{73 60}
Annealed									
MS 80725-1	2.8	0.30	{0.13 0.39}	0.39	{0.019 0.006}	6.4×10^{16}	{3.4×10^{17} 1.1×10^{17}}	9.2×10^{-19}	{5.2 5.1}
MS 80305-0	3.9	0.60	{0.13 0.39}	0.48	{0.035 0.011}	8.6×10^{16}	{1.0×10^{17} 3.1×10^{16}}	7.3×10^{-19}	{4.3 4.0}
MS 80725-13	5.0	0.90	{0.13 0.39}	0.57	{0.049 0.016}	3.2×10^{16}	{5.2×10^{17} 1.7×10^{17}}	5.3×10^{-19}	{25 23}
MS 80725-7	5.6	0.90	{0.13 0.39}	0.61	{0.047 0.015}	6.4×10^{16}	{2.8×10^{17} 8.9×10^{16}}	1.8×10^{-18}	{14 13}

[a]The two values listed in curly brackets correspond to taking the lower and upper bounds, respectively, of η_{ir}^a using the values obtained for crystal MS 80725-0 (see Table II).

increase in w (see Fig. 13). The constant s falloff of η_r^a at lower doping levels results from the rapid decrease in w with decreasing $N_A - N_D$ which dominates over the more slowly varying b_r [see Eq. (27)].

C. Internal Efficiency and Saturation

The above-gap excited internal quantum efficiencies of the red and infrared luminescence have been measured for a number of crystals of GaP(Zn, O). The variation of the red efficiency η_r^a with doping has been discussed with reference to Fig. 12. We have also observed a correlation between η_r^a and η_{ir}^a for these samples, i.e., a low infrared efficiency generally implies a low red efficiency and vice versa. This correlation suggests that the shunt path (the τ_n path of Fig. 1) is the major variable factor influencing the efficiency at constant doping levels. We also find that there appears to be little or no correlation between the amount of oxygen doping and the efficiencies η_r^a and η_{ir}^a. From this observation we conclude that the incorporation of oxygen into the GaP lattice during solution growth is uncontrolled.[30]

Of the crystals studied only one (MS 80725-0) was of sufficient thickness and optical quality for determination of the partial absorption coefficients for Zn-O and O. For this crystal the five measurements listed in Sec. II D have been performed, and the results (to be discussed in detail below) are summarized in Table II. We have also measured the above-gap efficiencies η_r^a and η_{ir}^a and the saturation of the red and infrared luminescence in four additional samples (see Table III) all with net acceptor concentration $N_A - N_D \approx 1.3\times10^{18}\,cm^{-3}$. For all five crystals we choose $w = 0.44$ in agreement with the model calculation for this doping level (see Fig. 13). In obtaining s from η_r^a for those samples listed in Table III we have used a calculated value of $b_r = 0.14$ in the relation $s = 1/[1 + w \times (b_r/\eta_r^a - 1)]$ [Eq. (27)]. To determine q for these samples we have assumed that η_{ir}^b [or b_{ir} ; see Eq. (29)] is the same for all crystals and have used upper and lower bounds corresponding to those measured for MS 80725-0. The concentrations N_t and N_0 have been calculated for the samples in Table III from the fit to the saturation data (to be described below) using a calculated lifetime $\tau_t = 0.24$ μsec and a measured lifetime $\tau_0 = 10$ μsec.[18]

At this point we discuss more fully the details of the measurement of η_r^b and η_{ir}^b and the fit to the saturation data. Discussion of the values obtained for the concentrations, capture cross sections, and minority carrier lifetime shown in Tables II and

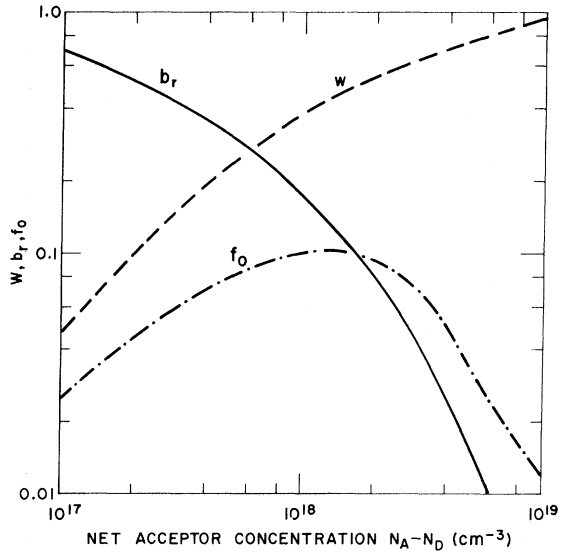

FIG. 13. Calculated dependence of w, b_r, and f_0 on the net acceptor concentration using the values of parameters given in Table I.

III is given in Sec. V D. To determine η_r^b and η_{ir}^b it is necessary to extract from the total optical absorption the partial absorption coefficients due to Zn-O and O impurities [recall Eqs. (46) and (47)]. Although these centers produce definite structure in the absorption spectra, there is difficulty in separating the known shapes of the individual bands from the background absorption. For example, in Fig. 4 the process responsible for absorption in the range 1.2–1.4 eV is expected to give a nonzero absorption coefficient when extrapolated into the region of oxygen absorption. Possible contributions to this background absorption will be discussed in a separate paper.[22] In obtaining the values of the below-gap efficiencies given in Table II, we have extrapolated the background in two different ways, thus giving upper and lower bounds for η_r^b and η_{ir}^b. We expect the true values of the parameters in Tables II and III to lie between the values listed and probably closer to the lower bound of η_{ir}^b.[31]

A typical set of saturation data is shown in Fig. 14. The data were taken using the focused 4880-Å output of an Ar^+ ion laser operating in the TEM_{00} mode. To minimize heating, the samples were immersed in a water bath. From a thermal analysis of the experimental geometry we estimate that the temperature rise of the sample is at most 5 °C above the bath temperature. The theoretical curves $L_r(g_e)$ and $L_{ir}(g_e)$ are obtained from the calculations discussed in Sec. II [recall Eqs. (35)–(38)] and are generated from the known values of s, q, and w for the crystal at hand. The experimental points are plotted versus the volume generation rate at the

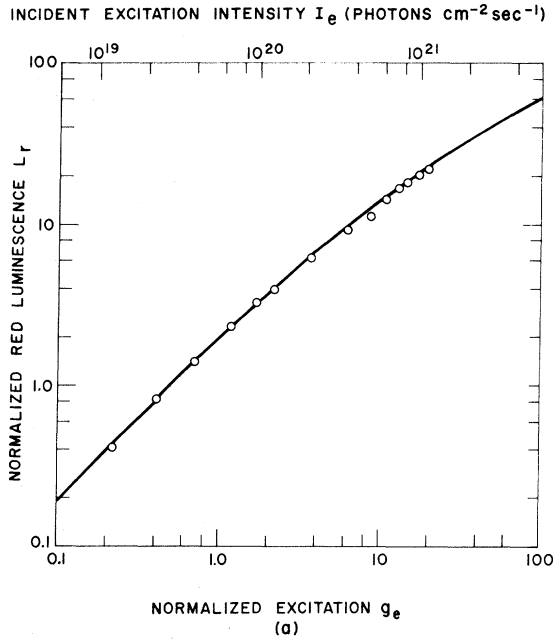

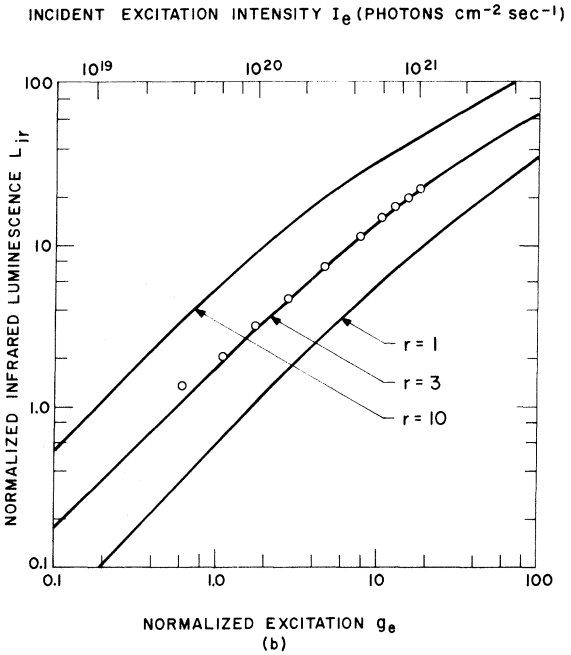

FIG. 14. Representative set of saturation data showing fit to calculated curves of L_r and L_{ir} versus normalized excitation g_e. (a) The red saturation data are fitted to the L_r curve, which is independent of the parameter r. This determines the ratio I_e/g_e. (b) Under this constraint the r curve of L_{ir} versus g_e is found which best fits the infrared saturation data. The ratios N_t/τ_t and N_0/τ_0 are determined from I_e/g_e and r as explained in the text.

surface $\alpha_e I_e$ [Eq. (35)]. The laser excitation flux I_e can be related to the total laser output P_e (photons/sec) by integrating Eq. (35) over the infinite half-plane, viz., $I_e = 2P_e/\pi\rho_0^2$. The half-width ρ_0 is determined by monitoring the laser power as a knife edge is moved through the beam at known positions. The output-versus-edge position follows an error-function dependence from which ρ_0 can be extracted. By matching the experimental points for the red luminescence to the theoretical saturation curve (both given as log-log plots), the ratio $\alpha_e I_e/g_e$ is obtained. Such a fit is shown in Fig. 14(a). The Zn-O concentration is thus determined by $N_t = \tau_t \alpha_e I_e/g_e$. For the sample of Table II we have calculated τ_t from a measured value of $\tau_{1/e} = 0.23$ μsec for the red luminescence (both as-grown and annealed) using Eq. (41) and the values of s shown. For the samples of Table III we use the calculated value $\tau_t = 0.24$ μsec. The absorption coefficient is $\alpha_e = 10^3$ cm^{-1}.[32] With the ratio of the abscissas $\alpha_e I_e/g_e$ of the calculated and experimental plots constrained by the fit to the red saturation data, the infrared data are matched with the r curve which gives the best fit. This fit is shown in Fig. 14(b). The O concentration is then determined by $N_0 = \tau_0 \alpha_e I_e/g_e r$. For the samples of Tables II and III we use a measured infrared decay time of $\tau_0 = 10$ μsec.

D. Discussion of Results

For the five crystals listed in Tables II and III, results have been obtained both in the as-grown state and after annealing for 5 h at 600 °C. We note that in as-grown material the substitutional oxygen concentration is of order 10^{17} cm^{-3}, and the Zn-O concentration is $(1.0-4.0)\times10^{16}$cm^{-3}. This value for oxygen is somewhat higher than found by other workers in solution-grown material,[33] whereas the Zn-O concentration is comparable to that estimated elsewhere.[4,7] A large fraction of the minority carrier recombination (as measured by s) proceeds via the Zn-O center, up to 80% in one case. A high s value is associated primarily with a long shunt path lifetime τ_n, the latter ranging from 5 to 70 nsec. This corresponds to electron diffusion lengths in the range 1–4 μ, which is in agreement with other work.[7,11] The low infrared efficiency results from a very low capture cross section for oxygen $\sigma_{n0} \sim 10^{-18}$ cm^2 two orders of magnitude smaller than the capture cross section for Zn-O. The small value of σ_{n0} is probably a consequence of the fact that the first excited state of the oxygen impurity is ~0.85 eV above the ground state.[34] Hence, phonon cascade[35] into the ground state is blocked by the large energy step required for the transition between the two lowest levels of the oxygen donor. Since the Zn-O state is shallower than the O ground state, such a large energy step is not required, making a larger cross section more likely.

Annealing is seen to increase the Zn-O concentration (through the promotion of ion pairing)[13,14] typically by a factor of 3–5. However, s and the red internal efficiency η_r^a typically increase only by 20%, and in two cases actually decrease with annealing (e.g., MS 80725-0 and MS 80725-7). This is explained by noting the drastic decrease in τ_n with annealing – by over a factor of 7 in the case of MS 80305-0. Since the recombination mechanism associated with τ_n is unknown, no explanation for its decrease with annealing is available. Empirically it should be noted, however, that the decreases in τ_n with annealing correlate with the increases in N_t. This is illustrated in the data of Fig. 15.

For three out of the five crystals investigated in Tables II and III the substitutional oxygen concentration *increases* with annealing. Since some of the oxygen is presumably associated with additional Zn-O pairs, an increase in O concentration implies a source of nonsubstitutional oxygen in the crystal, e.g., on interstitial sites or as Ga_2O_3 precipitates.[36] Futhermore, for those samples in which N_0 decreased, the magnitude of the decrease is not accounted for by the concentration of additional Zn-O pairs. The mechanism for the change in substitutional oxygen with annealing is, therefore, not understood, but presumably involves the background oxygen in the lattice. In corroboration of the saturation results, we show in Fig. 16 the effects of annealing on the absorption coefficient of MS 80725-0. Even without separating the partial absorption coefficients for Zn-O and O, it is evident

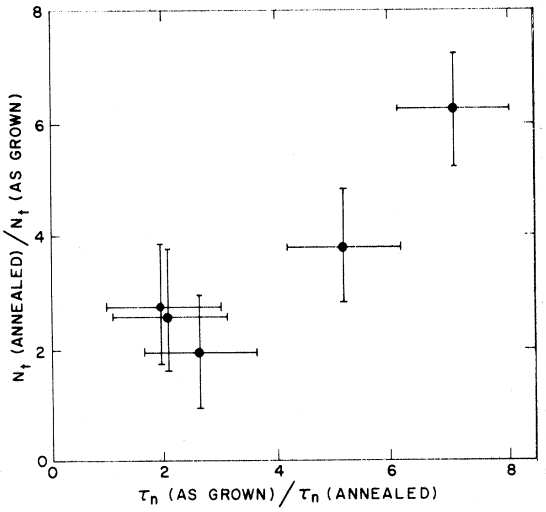

FIG. 15. Correlation between the increase in Zn-O concentration and the decrease in shunt path lifetime upon annealing.

from Fig. 16 that the absorption maximum due to oxygen (at 1.75 eV) is decreased upon annealing, while that due to Zn-O (at 2.13 eV) increases in agreement with the data of Tables II and III.

Finally, we note that changes in $\tau_{1/e}$, η_r^a, η_r^b, and η_{ir}^a upon annealing[15] can be understood on the basis of comparable changes in the s branching ratio, which enters crucially in the formulas for these parameters [Eqs. (27), (28), (30), and (41)]. Large changes in s can result from either large changes in the Zn-O complex concentration, or from changes in the shunt path lifetime τ_n. In this work, however, we find these effects are offsetting in going from the as-grown to the annealed state, resulting in only slight changes in s.

VI. DISCUSSION AND CONCLUSIONS

The results of Sec. V indicate that the room-temperature red internal quantum efficiency of GaP-(Zn-O) is limited primarily by the two Auger lifetimes τ_{xn} and τ_{en} [Eqs. (49) and (50)] and by thermalization of trapped electrons from Zn-O sites into the conduction band. As shown in Fig. 13, at high net acceptor concentrations the efficiency is limited by the falloff in b_r [recall Eq. (27)], while at low acceptor concentrations the efficiency is limited by w. The importance of the bare Auger lifetime τ_{en} at high $N_A - N_D$ stems from the lowered value of σ_{pt} due to plasma screening by the free holes. This acts to lower the fraction f_0 of exciton-occupied Zn-O sites. With f_0 small, a greater fraction of recombination traffic through Zn-O sites involves the bare electron states N_t^- for which the Auger lifetime is τ_{en}.

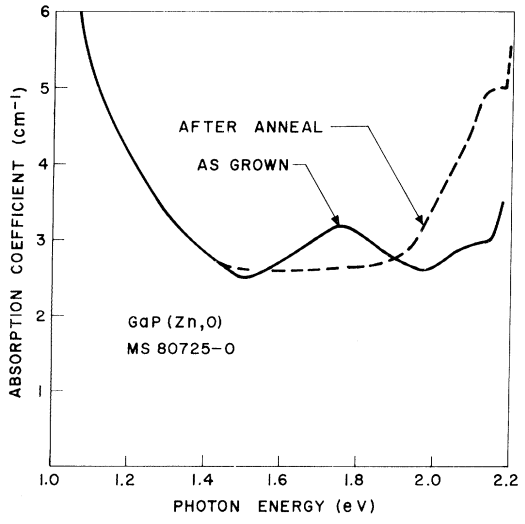

FIG. 16. The effect of annealing on the absorption spectrum of GaP(Zn,O). The decrease in O absorption and the increase in Zn-O absorption (cf. Fig. 4) are in agreement with the saturation results shown in Table II.

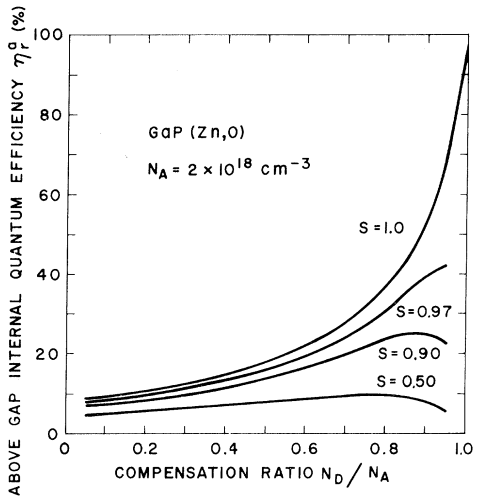

FIG. 17. Calculated improvement of red above-gap internal quantum efficiency by compensation for material in which $N_A = 2 \times 10^{18}$ cm^{-3}. The curves were generated using the values of parameters given in Table I.

For material in which thermalization is unimportant, i.e., in which s is near unity [recall Eq. (27)], we expect to be able to improve the red efficiency η_r^a by lowering $N_A - N_D$ through compensation and, as a consequence, reduce the Auger processes. In Fig. 17 we show the calculated effects of compensation on crystals for which $N_A = 2 \times 10^{18}$ cm^{-3}. Large gains in efficiency are obtained only for s values near unity and for high compensation ratios. An ultimate efficiency of 100% is possible only for $s = 1$ at complete compensation. For the samples studied in this work we find an upper bound of $s \approx 0.8$, which implies a possible bulk internal efficiency of approximately 20%. More typically, we find for $N_t \approx 5 \times 10^{16}$ cm^{-3} a value of $s \approx 0.5$ corresponding to $\tau_n \approx 10$ nsec, for which η_r^a can be maximized by compensation to 10% (Fig. 17). To increase η_r^a to 25% corresponding to $s = 0.9$, we must increase either τ_n or N_t by an order of magnitude. To gain an internal efficiency of up to 40% ($s = 0.97$ in Fig. 17) we must increase either τ_n or N_t by two orders of magnitude from their $s = 0.5$ values. Since such large increases in N_t are unlikely, these results indicate that elimination of the shunt is called for, presumably by the use of higher-purity GaP.

Because of the long total lifetime τ_t associated with the low hole concentrations at high compensation ratios (see Fig. 11), we expect saturation of the luminescence to occur at much lower excitation levels than observed for the samples of Tables II and III. In practical electroluminescent diodes the

electron injection efficiency is limited at low levels by space-charge recombination.[37] Thus, for such a device the bulk material efficiencies shown in Fig. 17 may not be realizable because of saturation at higher injection levels. Nevertheless, it does appear that high-efficiency red emitting diodes can be achieved simultaneously by (i) increasing the s branching ratio to $s \gtrsim 0.9$ through reductions in the τ_n shunt path, (ii) compensating to reduce the free-hole concentration and consequent Auger processes, and (iii) improving in p-n junction formation to optimize electron injection into the active p region.

ACKNOWLEDGMENTS

We wish to express our thanks to F. A. Trumbore and L. Derick for providing the crystals used in this study and to R. H. Saul for help in annealing. We gratefully acknowledge the help of K. P. Sinha in performing the calculation in Appendix D and acknowledge a number of beneficial discussions with L. J. Varnerin. We thank W. H. Hackett for his information on impurity concentrations. Finally, thanks are due E. F. Kankowski for his assistance in much of the experimental work.

APPENDIX A: THERMAL EMISSION RATES FOR ISOELECTRONIC CENTERS

We calculate here the rate e_{nt} for thermal emission of deeply trapped electrons out of N_t^- states into the conduction band and the rate e_{pt} for thermal emission of the weakly bound holes out of N_t^x states into the valence band. These rates are given by

$$e_{nt} = K_{nt}(N_t^-/N_t), \tag{A1}$$

$$e_{pt} = K_{pt}(N_t^x/N_t), \tag{A2}$$

where K_{nt} and K_{pt} are proportionality constants which we wish to determine. Under the condition of detail balance, the emission rates are equal to the corresponding capture rates at thermal equilibrium, where the capture rates are given by

$$r_{nt} = (n/\tau_{nt})(N_t^0/N_t)\ , \tag{A3}$$

$$r_{pt} = (p/\tau_{pt})(N_t^-/N_t). \tag{A4}$$

The required equality at thermal equilibrium results in

$$K_{nt} = (n_0/\tau_{nt})(N_t^0/N_t^-)_{eq}\ , \tag{A5}$$

$$K_{pt} = (p_0/\tau_{pt})(N_t^-/N_t^x)_{eq}\ . \tag{A6}$$

The thermal equilibrium values of the concentrations $N_t^0|_{eq}$, $N_t^-|_{eq}$, and $N_t^x|_{eq}$ are given by

$$N_t^0|_{eq} = [1 - f_{eq}(E_t')]N_t\ , \tag{A7}$$

$$N_t^-|_{eq} = f_{eq}(E_t')f_{eq}(E_h)N_t\ , \tag{A8}$$

$$N_t^x|_{eq} = f_{eq}(E_t')[1 - f_{eq}(E_h)]N_t, \tag{A9}$$

where $f_{eq}(E)$ is the thermal equilibrium probability for *electron* occupation at the energy level E (measured from the valence-band maximum) and is given by

$$f_{eq}(E) = (1 + \beta e^{(E-\varphi_0)/kT})^{-1}\ . \tag{A10}$$

In Eq. (A10), β is the degeneracy factor of the level at E, and φ_0 is the thermal-equilibrium Fermi level. In Eqs. (A7)–(A9), E_h is the binding energy of a hole to the charged isoelectronic center, and $E_t' = E_g - E_t$, where E_g is the band gap and E_t is the binding energy (below the conduction-band minimum) of the deeply trapped electron. In the nondegenerate case the thermal equilibrium concentrations of free electrons and holes, respectively, are given by

$$n_0 = N_c e^{(E_g-\varphi_0)/kT}\ , \tag{A11}$$

$$p_0 = N_v e^{-\varphi_0/kT}\ . \tag{A12}$$

Combining Eqs. (A5)–(A12) we find that

$$K_{nt} = (N_c/\tau_{nt})\beta_t e^{-E_t/kT}(1 + \beta_h e^{(E_h-\varphi_0)/kT})\ , \tag{A13}$$

$$K_{pt} = (N_v/\tau_{pt})\beta_h^{-1} e^{-E_h/kT}. \tag{A14}$$

Usually $e^{(E_h-\varphi_0)/kT} \ll 1$, so we approximate K_{nt} with

$$K_{nt} \cong (N_c/\tau_{nt})\beta_t e^{-E_t/kT}. \tag{A15}$$

Using Eqs. (A15) and (A14) in Eqs. (A1) and (A2), respectively, then leads to the definitions of n_t and p_h in Eqs. (4) and (8).

APPENDIX B: EXCITON OCCUPATION FACTOR FOR BELOW-BAND-GAP EXCITATION

When bound excitons are directly created at Zn-O sites by the absorbed below-gap excitation, the parameters b_r and w in Eq. (30) are slightly changed from their above-gap values. This results from a change in the exciton occupancy factor f_0 [Eq. (5)] which enters into the definitions of b_r [Eqs. (10) and (26)] and w [Eq. (18)]. Equation (3) was derived assuming that only N_t^- states were created from the neutral unoccupied states (of concentration N_t^0) by the incident radiation, i.e., the only process considered was

$$(\text{photon},\ N_t^0) \rightarrow (N_t^-,\ \text{free hole}). \tag{B1}$$

A second possible process is

$$(\text{photon},\ N_t^0) \rightarrow N_t^x. \tag{B2}$$

If we let σ^- and σ^x represent the respective photo cross sections for these processes, then the generation rate of bare-electron states due to the incident intensity I_e is $I_e\sigma^- N_t^0$, and for bound excitons is $I_e\sigma^x N_t^0$. The steady-state recombination is governed by the equations

$$I_e\sigma^- N_t^0 = N_t^-/\tau_\beta + (p/\tau_{pt})\ (N_t^-/N_t) - (p_h/\tau_{pt})\ (N_t^x/N_t)$$

$$+ (n_t/\tau_{nt})(N_t^-/N_t) - (n/\tau_{nt})(N_t^0/N_t), \quad \text{(B3)}$$

$$I_e\sigma^x N_t^0 = N_t^x/\tau_\alpha + (p_h/\tau_{pt})(N_t^x/N_t) - (p/\tau_{pt})(N_t^-/N_t), \quad \text{(B4)}$$

where

$$N_t = N_t^0 + N_t^- + N_t^x . \quad \text{(B5)}$$

We define $N_t^e \equiv N_t^- + N_t^x$ and let f_α be the fraction of total captured electrons on Zn-O sites which are incorporated as excitons, i.e., $N_t^x = f_\alpha N_t^e$ and $N_t^- = (1-f_\alpha)N_t^e$. Making these substitutions and eliminating N_t^e between Eqs. (B3) and (B4), we obtain in the low excitation limit $[I_e(\sigma^- + \sigma^x)N_t^0 \ll N_t^e/\tau_t]$

$$f_\alpha = \frac{p/\tau_{pt} + (\sigma^x/\sigma^e)(N_t/\tau_\beta) + (1-s)(\sigma^x/\sigma^e)(n_t/\tau_{nt})}{(p+p_h)/\tau_{pt} + (1+\sigma^x/\sigma^e)(N_t/\tau_\alpha) + (\sigma^x/\sigma^e)(N_t/\tau_\beta)},$$

where $\sigma^e \equiv \sigma^x + \sigma^-$. It is easily seen that for $\sigma^x = 0$, $f_\alpha = f_0$, where f_0 is given by Eq. (5). In general, however, if σ^x is nonvanishing then the fraction of exciton-occupied Zn-O sites is larger for below-gap excitation. Since τ_t, τ_r, b_r, and w all depend on f_0 or f_α through Eqs. (10), (18), and (26), these parameters will also differ between the two cases. We have estimated the increase in b_r, and in f_α over f_o for values of $N_A - N_D$ appropriate to the samples listed in Tables II and III. We find that f_α is at most 60% larger than f_0, which results in a 30% increase in b_r from its above-gap value. Since this increase is within the experimental error of determining η_r^b (see Appendix C), it has been neglected in obtaining the values listed in Tables II and III.

APPENDIX C: DETERMINATION OF INTERNAL QUANTUM EFFICIENCY AND LIMITS OF ERROR

The internal quantum efficiency can be determined by measurement of the surface radiance on samples with parallel plane geometry (see Fig. 5). To calculate the radiance $\mathcal{R}_\theta$ we decompose the volume of the crystal enclosed by the internal solid angle $d\Omega'$ into a series of truncated cones whose bases lie on the front and back surfaces, as indicated in Fig. 18(a). To obtain $\mathcal{R}_\theta$ we compute the fraction of the internal luminescence generated in the kth cone that reaches $d\Omega$ after undergoing $k-1$ reflections and suffering attenuation by $k-1$ path lengths. $\mathcal{R}_\theta$ is then calculated by summing over all the cones. More explicitly, if we let $\mathcal{L}_k(E)$ represent the fraction of the total internal luminescence with photon energy E generated in the kth cone and exiting the crystal across dA through $d\Omega$, we obtain

$$\mathcal{R}_\theta = \int_{E_1}^{E_2} dE\,[(1-R_{\theta'})/dA\,d\Omega]\sum_{k=1}^{\infty}(R_{\theta'})^{k-1}$$

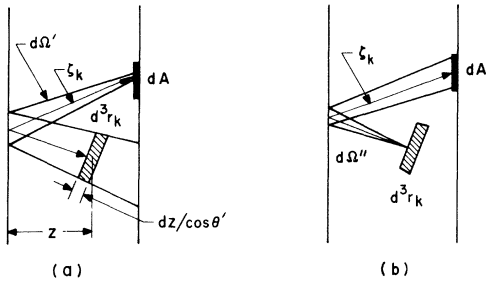

FIG. 18. Relationship between the volume element and the solid angles used for the radiance calculation. (a) Definition of d^3r_k as the intersection of the cone $d\Omega'$ and the slab of thickness $dz/\cos\theta'$ (cf. Fig. 5). (b) Definition of $d\Omega''$ as the solid angle subtended by the area dA at the volume element d^3r_k separated from dA by a distance ζ_k.

$$\times \exp[-(k-1)\alpha d/\cos\theta']\,\mathcal{L}_k(E). \quad \text{(C1)}$$

In this expression $R_{\theta'}$ and α are, respectively, reflection and absorption coefficients for the radiation emitted at photon energy E, and (E_1, E_2) is the energy interval of the luminescent band. To calculate $\mathcal{L}_k$ we consider the volume element d^3r_k in the kth cone at a distance z from the front surface as shown in Fig. 18(b). The thickness of this element is $dz/\cos\theta'$ and its area is $d\Omega'\zeta_k^2$, where ζ_k is the distance from d^3r_k to dA measured along the axis of $d\Omega'$. In Fig. 18(b) we also consider the solid angle $d\Omega'' = dA\cos(\theta')/\zeta_k^2$ which is subtended by dA at d^3r_k with axis along $d\Omega'$. If we let $l(z, E)$ be the volume photon generation rate into 4π sr at energy E and position z, then we obtain

$$\mathcal{L}_k = \int_{V_k} d^3r_k \exp(-\alpha z/\cos\theta')\,l(z, E)\,d\Omega''/4\pi, \quad k \text{ even}, \quad \text{(C2)}$$

$$\mathcal{L}_k = \int_{V_k} d^3r_k \exp[-\alpha(d-z)/\cos\theta']\,l(z, E)\,d\Omega''/4\pi, \quad k \text{ odd}.$$

In Eqs. (C2) V_k is the volume of the kth cone, and the exponential factor expresses the attentuation due to the path length from d^3r_k to the preceding cone. By combining Eqs. (C1) and (C2) and changing variables in the integral from d^3r_k to $dz\,d\Omega'\zeta_k^2/\cos\theta'$, we obtain

$$\mathcal{R}_\theta = \frac{1}{4\pi n^2}\int_{E_1}^{E_2} dE \int_0^d dz\,\{\exp[-\alpha(d-z)/\cos\theta'] + R_{\theta'}\exp[-\alpha(d+z)/\cos\theta']\} \times \left(\frac{(1-R_{\theta'})}{1-R_{\theta'}^2\exp(-2\alpha d/\cos\theta')}\right)\frac{\cos\theta}{\cos\theta'}\,l(z, E)\,. \quad \text{(C3)}$$

To calculate $\mathcal{R}_\theta$ we express $l(z, E)$ in terms of the incremental internal quantum efficiency $\eta(E)$ for emission of photons of energy E. In the case of excitation above the band gap we have

$$l(z, E) = \eta^a(E) n(z)/\tau_m , \tag{C4}$$

where $n(z)$ gives the spatial distribution of the minority carriers and τ_m is their total lifetime. DeVore[38] has solved for the distribution $n(z)$ in a geometry similar to that considered here and found that

$$n(z) = \frac{(1-R_a)\,\alpha_a I_a \tau_m}{(1-\alpha_a^2 L_D^2)}\,(e^{-\alpha_a z} + Be^{z/L_D} + Ce^{-z/L_D}), \tag{C5}$$

where L_D is the diffusion length of minority carriers, and R_a, α_a, and I_a refer to the reflection coefficient, absorption coefficient, and incident intensity of the above-gap excitation, respectively. The coefficients B and C are functions of L_D, α_a, τ_m, d, and the surface recombination velocity v_s. The above result neglects multiple internal reflection of the excitation, which is a good assumption for $\alpha_a d \gg 1$. For crystals similar to the ones investigated here, other workers[11,39] have found at room temperature that $L_D \approx 1\ \mu$ and $v_s\tau_m/L_D \gg 1$. Combining these results with the values[30] of $\alpha_a \approx 10^3\ \mathrm{cm}^{-1}$ (for 4880-Å excitation) and $d \approx 0.04$ cm, we may reduce Eq. (C5) to a form independent of L_D and v_s. When this is done and the result substituted into Eq. (C3), we obtain the radiance for excitation above the band gap assuming $\alpha_a \gg \alpha/\cos\theta'$:

$$\mathcal{R}_\theta = \frac{(1-R_a)}{4\pi n^2}\left(\frac{\cos\theta}{\cos\theta'}\right) I_a \int_{E_1}^{E_2} dE\,(1-R_{\theta'}^2) \times \left(\frac{\exp(-\alpha d/\cos\theta')}{1-R_{\theta'}^2\exp(-2\alpha d/\cos\theta')}\right)\eta(E).$$

The crystals used in this study were selected to be free of gross optical inhomogeneities. One such sample polished on six sides to form a parallelepiped showed no evidence of internal scattering when examined with a He-Ne laser. However, some scattering was noted at the crystal surfaces where the beam entered and exited the sample. In addition, when the surfaces of this and other samples investigated were roughened through etching or coarse mechanical polishing, the measured radiance typically increased by a factor of 2. To check the effect of surface scattering on the radiance results, a measurement was made of the external quantum efficiency of the rectangular parallelepiped. The sample was mounted at the center of a calibrated integrating sphere and was excited by 4880-Å laser radiation focused into a rectangular cross section that just matched the largest surface of the sample. For such a geometry it is a straighforward matter to calculate the ratio of external quantum efficiency $\eta_{\mathrm{ext}}/\eta_{\mathrm{int}}$ from a knowledge of the average self-absorption coefficient for the emitted luminescence, the sample dimensions, and the index of refraction.[40] For our sample this yielded a calculated value of $\eta_{\mathrm{ext}}/\eta_{\mathrm{int}} = 0.08$. This compares with a measured value of 0.10. Since the results agree within the combined experimental error of ± 20% for both the internal and external measurements, we conclude that surface scattering is of negligible importance in obtaining η_{int} from the radiance data.

APPENDIX D: EFFECTS OF PLASMA SCREENING ON EXCITON RADIATIVE LIFETIME

Excitons form at isoelectronic Zn-O complexes by a two-step process in which (i) electrons are trapped at the complex, and (ii) holes are captured by Coulomb attraction into a shallow effective-mass state. A description of the resulting bound exciton is extremely difficult, especially when we recognize that the trapped electron state ($E_t \approx 0.23$ eV) is almost completely determined by the short-range (central-cell) potential associated with the deep O donor in the Zn-O complex, and the shallow ($E_h \approx 0.036$ eV) effective-mass hole state is made up of valence-band states. To calculate the effect of plasma screening on the bound-exciton lifetime we use a simple atomic model where the electron is an s state and the hole is in a p state, thus ensuring that the excitonic decay proceeds via an allowed electric dipole transition. Since the hole binding energy E_h decreases with increasing hole concentration as a result of screening [see Eq. (53)], we expect the hole wave function to become more extended, and, as a consequence, the dipole matrix element should decrease. The net effect should therefore be an increase in exciton lifetime with increasing hole concentration.

The wave functions for electrons in s states ψ_e and holes in p states ψ_h are

$$\psi_e = (\beta_e^3/\pi)^{1/2}\exp(-\beta_e r), \tag{D1}$$

$$\psi_h = (\beta_h^3/32\pi)^{1/2}\beta_h r\cos\theta\exp(-\beta_h r/2), \tag{D2}$$

where β_e and β_h are reciprocal Bohr radii. Since the electron is deeply trapped we expect β_e given by

$$\beta_e^2 = 2m_e^* E_t/\hbar^2 \tag{D3}$$

to be insensitive to screening, whereas β_h given by

$$\beta_h^2 = 2m_h^* E_h/\hbar^2 \tag{D4}$$

should change with doping in accord with Eq. (53). In Eqs. (D3) and (D4) m_e^* and m_h^* are the electron and hole effective masses, respectively. The dipole matrix element μ_x between states ψ_e and ψ_h is

$$\mu_x = e\beta_h(\beta_e^3\beta_h^3/32\pi^2)^{1/2}\int_V r^2\cos^2\theta \times \exp[-(\beta_e+\beta_h/2)r]\,d^3r\,. \quad \text{(D5)}$$

This is easily integrated to give

$$\mu_x = \left(\frac{e}{\pi}\right)(32\pi^2)^{1/2}\frac{\beta_e^{3/2}\beta_h^{5/2}}{(\beta_e+\beta_h/2)^5}\,. \quad \text{(D6)}$$

Note that since $E_t \gg E_h$, $\beta_e \gg \beta_h$ and thus Eq. (D6) reduces to

$$\mu_x \approx (e/\pi)(32\pi^2)^{1/2}(\beta_h^{5/2}/\beta_e^{7/2})\,. \quad \text{(D7)}$$

The excitonic transition rate $1/\tau_{xr}$ is proportional to $|\mu_x|^2 \propto \beta_h^5$. As a result, the ratio of screened to unscreened transition rates is given by

$$\frac{1/\tau_{xr}}{1/\tau_{xr}^0} = \frac{\beta_h^{\,5}}{\beta_h^{0}}\,, \quad \text{(D8)}$$

where the superscript 0 applies to the unscreened case. Combining Eqs. (D4) and (D8) we find that the intrinsic exciton lifetime scales with hold binding energy according to

$$\tau_{xr}/\tau_{xr}^0 = (E_h^0/E_h)^{5/2}\,, \quad \text{(D9)}$$

where E_h is given by Eq. (51).

---

[1]P. J. Dean, C. H. Henry, and C. J. Frosch, Phys. Rev. 168, 812 (1968).

[2]J. M. Dishman, Bull. Am. Phys. Soc. 15, 348 (1970); unpublished; R. N. Bhargava, Phys. Rev. B 2, 387 (1970).

[3]T. N. Morgan, B. Welber, and R. N. Bhargava, Phys. Rev. 166, 751 (1968); C. H. Henry, P. J. Dean, and J. D. Cuthbert, *ibid.* 166, 754 (1968).

[4]J. D. Cuthbert, C. H. Henry, and P. J. Dean, Phys. Rev. 170, 739 (1968).

[5]J. M. Dishman and M. DiDomenico, Jr., Phys. Rev. B 1, 3381 (1970).

[6]W. Shockley and W. T. Read, Jr., Phys. Rev. 87, 835 (1952); R. N. Hall, *ibid.* 87, 387 (1952).

[7]Our model for the minority carrier recombination can be viewed as a generalization of earlier work by W. Rosenzweig, W. H. Hackett, Jr., and J. S. Jayson, J. Appl. Phys. 40, 4477 (1969); see also, W. H. Hackett, Jr., W. Rosenzweig, and J. S. Jayson, Proc. IEEE 57, 2072 (1969).

[8]K. P. Sinha and M. DiDomenico, Jr., Phys. Rev. B 1, 2623 (1970).

[9]At liquid-helium temperatures $E_t \approx 0.3$ eV (Refs. 3 and 4).

[10]An upper bound of $E_t = 0.28$ eV is obtained by assuming that the exciton no-phonon line falls midway between the room-temperature maxima of the emission and absorption bands [M. DiDomenico, Jr. and J. M. Dishman (unpublished)]. A lower bound of $E_t = 0.18$ eV is obtained by taking the no-phonon line of exciton emission to lie at the upper limit of the red emission band, i.e., at ≈ 2.05 eV [see Fig. 8(b)].

[11]Neglecting thermalization effects, values of σ_{nt} in the range $1-5\times10^{-16}$ cm^2 have been obtained in Ref. 7, and by J. S. Jayson, J. Appl. Phys. (to be published).

[12]B. Welber and T. N. Morgan, Phys. Rev. 170, 769 (1968).

[13]A. Onton and M. R. Lorenz, Appl. Phys. Letters 12, 115 (1968).

[14]On the basis of an ion-pairing model of H. Reiss, C. S. Fuller, and F. J. Morin [Bell System Tech. J. 35, 535 (1950)], J. D. Wiley and J. A. Seman [Bell System Tech. J. 49, 355 (1970)] have shown that over 50% of substitutional O in GaP can be paired as Zn-O complexes for $N_A \approx 10^{18}$ cm^{-3}, $N_0 = 10^{17}$ cm^{-3} (cf. Tables II and III).

[15]This result has also been obtained by J. S. Jayson, R. N. Bhargava, and R. W. Dixon, J. Appl. Phys. (to be published).

[16]This method is similar to that used by J. Vilms and W. E. Spicer, J. Appl. Phys. 36, 2815 (1965).

[17]The overlap between the red and infrared luminescence bands was first inferred by R. N. Bhargava using time-decay measurements.

[18]The experimental time-decay data were provided by R. N. Bhargava.

[19]Similar saturation curves have been generated by J. S. Jayson (Ref. 11), using a two-path model, including the diffusion of minority carriers, but not thermalization effects. In our analysis diffusion is neglected, since the penetration depth of the excitation is found to be longer than the diffusion length. The importance of thermalization for saturation measurements is shown in Eq. (32).

[20]See, for example, J. F. Miller, in *Compound Semiconductors*, edited by R. K. Willardson and H. L. Goering (Reinhold, New York, 1962), Vol. 1, Chap. 23.

[21]Our definition of lifetime follows the convention of J. S. Blakemore, *Semiconductor Statistics* (Pergamon, New York, 1962).

[22]J. M. Dishman and M. DiDomenico, Jr. (unpublished).

[23]The generalization of our earlier result [Eq. (40)] to include the factor $(1-s)$ was first obtained by Jayson *et al.* (see Ref. 15).

[24]M. Gershenzon, F. A. Trumbore, R. M. Mikulyak, and M. Kowalchik, J. Appl. Phys. 37, 483 (1966).

[25]V. L. Bonch-Bruevich, Zh. Eksperim. i Teor. Fiz. 32, 1092 (1957) [Soviet Phys. JETP 5, 894 (1957)].

[26]The importance of screening on the radiative lifetime τ_{xr} was first pointed out by Jayson *et al.* (private communication). In Ref. 15 an independent calculation of τ_{xr} is presented which, however, gives the result $\tau_{xr} = \tau_{xr}^0(E_h^0/E_h)^{3/2}$.

[27]A. S. Barker, Jr. (private communication).

[28]W. H. Hackett, Jr., and R. N. Bhargave, J. Appl. Phys. 41, 3306 (1970).

[29]Two mechanisms can be postulated to explain this effect. In the first, an unknown donor impurity is incorporated into the lattice in proportion to the acceptor concentration. The minority carrier capture rate into this impurity is proportional to its concentration N_x. Hence, $1/\tau_n \propto N_x \propto N_A$. For the second mechanism, we

assume that an unknown deep acceptor impurity remains at a constant background value N_x with Zn doping. If capture into this center proceeds via an Auger process whereby a free hole is ejected deep into the valence band, then $1/\tau_n \propto N_x p \propto N_x N_A$.

[30]T. Miyanchi, H. Sonomura, and N. Yamamoto, J. Appl. Phys. (Japan) 8, 886 (1969).

[31]The temperature dependence of η_{ir}^{b} for these crystals has been measured [J. M. Dishman (Ref. 2)] and appears very similar to that observed for η_{ir}^{a} in Fig. 7. The thermal quenching of η_{ir}^{b} is best explained by taking the lower value $\eta_{ir}^{b}=0.13$ in Tables II and III.

[32]W. G. Spitzer, M. Gershenzon, C. J. Frosch, and D. F. Gibbs, J. Phys. Chem. Solids 11, 339 (1959).

[33]L. M. Foster and J. Scardefield, J. Electrochem. Soc. 116, 494 (1969).

[34]P. J. Dean and C. H. Henry, Phys. Rev. 176, 928 (1968).

[35]M. Lax, Phys. Rev. 119, 1502 (1960).

[36]C. K. Kim [Radiochem. Radioannal. Letters 2, 53 (1969)] has found *total* oxygen concentrations of 2×10^{19} cm^{-3} in O-doped solution-grown crystals of GaP comparable to those studied here. M. Kowalchik (unpublished) has found Ga_2O_3 precipitates in GaP(Zn, O) layers grown by liquid-phase epitaxy. Both results suggest the probability of large concentrations of nonsubstitutional O in these samples.

[37]M. Gershenzon, R. A. Logan, and D. F. Nelson, Phys. Rev. 149, 580 (1966).

[38]H. B. DeVore, Phys. Rev. 102, 86 (1956).

[39]M. Gershenzon and R. M. Mikulyak, Appl. Phys. Letters 8, 245 (1966).

[40]W. Bond (unpublished).

PHYSICAL REVIEW B VOLUME 2, NUMBER 6 15 SEPTEMBER 1970

Magnetoresistance and Hall Effect of Hot Electrons in Germanium and Carrier Transfer to Higher Minima*

H. Heinrich and K. Lischka

Institut für Angewandte Physik der Universität, A-1090 Vienna, Austria and Ludwig Boltzmann Institut für Festkörperphysik, Vienna, Austria

and

M. Kriechbaum†

Institut für Theoretische Physik der Universität, A-8010 Graz, Austria

(Received 15 January 1970)

Measurements are reported of the Hall coefficient and the ratio of longitudinal over transverse magnetoresistance in n-type Ge up to electric field strengths of 3 and 9 kV/cm, respectively, for $\vec{j} \parallel [100]$ at 200 °K, in order to obtain quantitative information about electron transfer to higher conduction-band minima. The lattice temperature was high enough to ensure that no negative differential conductivity was present. Calculations of the galvanomagnetic properties have been performed for the case that (i) electrons are only in the normally occupied ⟨111⟩ valleys, taking into account acoustical, optical, and equivalent intervalley scattering as well as scattering by ionized impurities; and (ii) electrons are transferred to the higher ⟨100⟩ conduction-band minima. Only in case (ii) is reasonable agreement between theoretical and experimental results obtained, giving a mobility ratio of only about 4. This is of the same order of magnitude as the theoretical value by Paige.

I. INTRODUCTION

As is well known, the conduction band of germanium consists of four normally occupied minima along the ⟨111⟩ directions in k space, another minimum at the center of the Brillouin zone, and a third set of six minima along the ⟨100⟩ axis approximately 0.18 eV above the lowest minima.[1,2] In the past, these higher minima have been considered in influencing the high-field behavior of n-type Ge.[3–5] Recently, they have been made responsible, by Fawcett and Paige,[6,7] for giving rise to the bulk negative differential resistance[8] (NDR) by a mechanism similar to that of the Gunn effect in GaAs and to the associated current oscillations observed by McGroddy and Nathan.[9] It is, however, not yet established[10] whether the influence of the carrier transfer alone is strong enough to cause the NDR or another effect is responsible for it (e.g., Kawamura and Morishita[11] and Gueret[12]).

It is the purpose of this paper to present an experimental indication that population of higher val-